THE STUDY OF QUASI-PERIODIC OSCILLATIONS FROM SOFT GAMMA REPEATERS

Joanne Kettner

Master of Science

Department of Physics

McGill University

Montréal, Québec

2007-09-17

A thesis submitted to McGill University in partial fulfilment of the requirements of the degree of Master of Science

Library and
Archives Canada

Published Heritage
Branch

395 Wellington Street
Ottawa ON K1A 0N4
Canada

Bibliothèque et
Archives Canada

Direction du
Patrimoine de l'édition

395, rue Wellington
Ottawa ON K1A 0N4
Canada

Your file Votre référence
ISBN: 978-0-494-38408-4
Our file Notre référence
ISBN: 978-0-494-38408-4

NOTICE:
The author has granted a non-exclusive license allowing Library and Archives Canada to reproduce, publish, archive, preserve, conserve, communicate to the public by telecommunication or on the Internet, loan, distribute and sell theses worldwide, for commercial or non-commercial purposes, in microform, paper, electronic and/or any other formats.

The author retains copyright ownership and moral rights in this thesis. Neither the thesis nor substantial extracts from it may be printed or otherwise reproduced without the author's permission.

AVIS:
L'auteur a accordé une licence non exclusive permettant à la Bibliothèque et Archives Canada de reproduire, publier, archiver, sauvegarder, conserver, transmettre au public par télécommunication ou par l'Internet, prêter, distribuer et vendre des thèses partout dans le monde, à des fins commerciales ou autres, sur support microforme, papier, électronique et/ou autres formats.

L'auteur conserve la propriété du droit d'auteur et des droits moraux qui protège cette thèse. Ni la thèse ni des extraits substantiels de celle-ci ne doivent être imprimés ou autrement reproduits sans son autorisation.

In compliance with the Canadian Privacy Act some supporting forms may have been removed from this thesis.

While these forms may be included in the document page count, their removal does not represent any loss of content from the thesis.

Conformément à la loi canadienne sur la protection de la vie privée, quelques formulaires secondaires ont été enlevés de cette thèse.

Bien que ces formulaires aient inclus dans la pagination, il n'y aura aucun contenu manquant.

Canada

ACKNOWLEDGEMENTS

I thank Matt Becker, Caroline Niquette, and my mother for their support throughout my degree. I thank Paula Domingues for being so helpful and patient, and Elizabeth Shearon for being so giving over the past two years. I also thank my supervisor, Andrew Cumming.

ABSTRACT

Hyperflares from Soft Gamma Repeaters have revealed quasi-periodic oscillations, suggested to be torsional modes of the neutron star crust produced during starquakes. We study how a magnetic field affects these modes. We make a plane-parallel model of the neutron star crust with a vertical and non-vertical field and solve for the eigenvalues and eigenfunctions. In the vertical field case we find a discrete set of modes comparable to the observed frequencies giving evidence for this theory. We find that the lower order modes do not depend on B while the higher order modes do when the field strength is low or extremely high. We make a simple analytic model of a non-vertical field in a closed box representing the neutron star crust. The mode spectrum in this model is continuous rather than discrete, raising the puzzle of why only specific modes are excited during the hyperflare.

ABRÉGÉ

Des sursauts géants provenant de sursauteurs gamma mou ont révélé des oscillations quasi-périodiques qui pourraient être des modes de torsion produits durant les tremblements de la croûte d'une étoile à neutrons. Nous étudions comment un champ magnétique affecte ces modes. Nous produisons un modèle d'une étoile à neutrons avec un champ vertical et non-vertical puis nous solutionnons pour trouver les valeurs propres. Dans le cas du champ vertical, nous trouvons une série discrète de modes comparables aux fréquences observées. Nous trouvons que les modes de bas ordres ne dépendent pas de B alors que les modes d'ordres plus élevés en dépendent parfois. Nous produisons un modèle analytique d'un champ non-vertical dans une boîte fermée qui représente la croûte de l'étoile à neutrons. Le spectre des modes dans ce modèle est continu plutôt que discret ce qui nous amène à nous demander pourquoi seuls des modes spécifiques sont excités durant les sursauts géants.

TABLE OF CONTENTS

LIST OF TABLES

LIST OF FIGURES

CHAPTER 1
Introduction

1.1 Overview

A neutron star is born after a Type Ib, Ic, or II supernova explosion, caused by the collapse of an $\sim 8-60\ M_{\odot}$ star (the upper mass limit is uncertain and depends on metallicity; Heger et al. 2003), where $M_{\odot} = 1.99 \times 10^{33}$ g is one solar mass (Hansen et al. 2004, Shapiro & Teukolsky 1983). It should be noted that neutron stars are not the only stars born after Type II supernovae sometimes a black hole is born. When the newly formed star is a neutron star it has the following properties; a mass $\approx 1.2 - 1.4\ M_{\odot}$ (Heger et al. 2003), a radius of $\sim 10^6$ cm, and an extremely high mean density of $\lesssim 10^{15}$ g cm^{-3}. After the superova explosion, the neutron star may be spinning extremely rapidly, depending on whether angular momentum of the core is conserved during stellar evolution and collapse (Heger et al. 2005). Eventually the star's period will decrease at a very slow rate as its rotating magnetic field radiates energy away.

Neutron stars are composed of layers. See Figure (1–1) for a cross sectional slice of the different regions (Shapiro & Teukolsky 1983). The innermost section is an extremely dense fluid core tightly packed with neutrons, protons, and electrons. The exact structure at the center is currently unknown and of great interest to many theoretical physicists, with suggestions ranging from pion condensates to quark matter to a neutron solid. The next layer is a solid crust which forms as the pressure and temperature decrease outside the core. This crust has an inner and outer region. The inner crust contains nuclei, free neutrons, and free electrons while the outer crust is composed of free electrons and nuclei that decreases in neutron number the further it gets from the star's center. The outermost layer is a fluid ocean consisting of iron and neutron rich isotopes (Hansen et al. 2004).

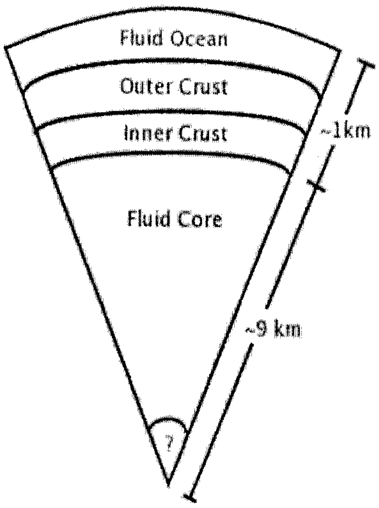

Figure 1–1: Cross sectional slice of the layers within a neutron star.

There are many different types of neutron stars. Those of interest for this dissertation are magnetars (Duncan & Thompson 1992, Thompson & Duncan 1995). A magnetar is thought to be born when its parent star has a fast rotation rate and an extremely large surface magnetic field before exploding as a supernova. The birthrate for these stars in our Galaxy is estimated to be $\sim (1 - 10) \times 10^{-4}$ yr^{-1} (Duncan & Thompson 1992, Thompson & Duncan 1995). These young isolated neutron stars have long rotation periods ($\sim 5 - 12$ s) and extremely strong magnetic fields ($\sim 10^{14} - 10^{15}$ G) compared to other types of neutron star. As a result of these field strengths the main source of free energy in magnetars is magnetic as opposed to rotational.

There exist at least two kinds of magnetars, Soft Gamma Repeaters (SGRs) and Anomalous X-ray Pulsars (AXPs). The former will be the focus of this dissertation. SGR bursts come in two forms, regular and giant. The giant bursts (or flares) are also referred to as hyperflares in the literature. Both bursts arise when the magnetic energy within the star becomes so strong it cracks the crust and emits high energy Alfvén waves into the magnetosphere, mostly in the form of gamma rays and x-rays (Thompson & Duncan 1995). The regular flares are thought to be powered by magnetic field diffusion across small crustal fractures, whereas the giant flares are expected to be produced through a sudden shift and reconnection of the magnetic field causing large fractures in the crust which in turn lead to the emission of extremely powerful Alfvén waves.

There have been three hyperflares observed to date, each of which has revealed quasi-periodic oscillations (QPOs) in addition to their spin periods. The implication of these oscillations is that we are detecting toroidal (or torsional) modes produced by seismic vibrations within the neutron star crust (Duncan 1998). It is expected that these starquakes would produce many different modes as waves pass radially through the crust and circularly around it. The main restoring forces for these modes arise from the Coulomb forces between the ions within the solid crust. Because these forces are relatively weak these modes are easy to excite, where the lowest order modes are those most likely to be excited. Some other reasons these low order modes are expected to be excited is that they have a slow damping rate due to their long periods and they are closer to the stellar surface than other modes, which enables them to couple to the external magnetic field more easily (Blaes et al. 1989).

Seismology, the study of seismic waves from earthquakes, has been used to learn about properties of the Earth. Global shear modes were detected in the Earth after an earthquake in 1960, and a fundamental period of 43 minutes was found (Duncan 1998). Other toroidal modes have since been found in the Earth. Another form of seismology, helioseismology, has been used to study solar oscillation frequencies which has given insight into the structure of the solar interior (Hansen et al. 2004). If in fact we are observing seismic vibrations of neutron star crusts during magnetar flares this is extremely exciting as we can now use seismology to gain a better understanding of neutron stars!

The focus of this dissertation will be on QPOs produced by SGRs. We will begin by covering the observations of the SGR regular and giant flares (section 1.2), followed by a summary of the theoretical work describing these objects and their giant bursts (section 1.3). In Chapter 2 we will describe the theory behind torsional modes of the neutron star crust, comparing our results to the work done by Piro (2005) on this subject. In Chapter 3 we will take this subject a bit further by considering a more complicated field geometry. We will end this chapter by giving an overview of what will be covered in the rest of the dissertation.

1.2 Observations of SGRs

There are currently five known SGRs, four in our galaxy and one in the Large Magellanic Cloud (LMC). The first detection of these objects was in 1979 (Mazets et al. 1979a) and bursts are still being observed today. They were not given the name Soft Gamma Repeaters until 1986 when they were classified as a distinct set of objects, differing from the other bursters (Woods & Thompson 2006). These stars have many distinguishing properties. They produce frequent gamma-ray flares (peak luminosities of $L_{peak} \approx 10^{41}$ ergs s^{-1}) and on rare occasions giant flares which produce extraordinary amounts of energy ($L_{peak} \approx 10^{44} - 10^{46}$ ergs s^{-1}) (Duncan & Thompson 1992). These giant bursts begin with a hard spike of spectrally soft gamma-rays, lasting anywhere from a fraction of a second to a few seconds, followed by a weaker decaying tail that can continue for a few hundred seconds. See Figure (14.6) in the paper by Woods & Thompson (2006) which shows the giant burst emitted from SGR 1900+14 using data from a detector on Ulysses. SGRs are capable of emitting many bursts, differing from supernovae and gamma ray bursts which only release one explosion throughout their lifetimes (Woods & Thompson 2006). Their observed periods are between 5 and 8 seconds. We proceed by giving the details of the detections and analysis of the five currently known SGRs.

1.2.1 SGR 0526-66, The March 5th Event

The first giant flare was detected on March 5th 1979 and it came from the source SGR 0526-66 (Mazets et al. 1979a). Its location is 180 000 light years from our galaxy in a young ($\sim 10^4$ yr) supernova remnant (SNR N49) in the LMC (Cline et al. 1982). When the source was detected there was an initial hard pulse of gamma rays that lasted for $\sim$0.2 s, followed by a soft tail of less intense gamma rays lasting for more than three minutes. This observation was extremely exciting as it was the most energetic flare of gamma rays ever to be recorded, and had an isotropic energy of $\approx 5 \times 10^{44}$ ergs (Woods & Thompson 2004). Over the next two months this source emitted three regular bursts, the first lasting 1.5 s and the second and third lasting roughly 0.2 s. SGR 0526-66 continued to be active, emitting 16 more bursts, until May 1983. Since then there have been no detections from this source.

The original hyperflare was recorded by ten different spacecrafts; two Soviet interplanetary space probes Venera 11 and Venera 12; the American space probe Helios 2; the Pioneer Venus Orbiter's gamma ray detector; three Vela satellites; the Soviet satellite Prognoz 7; an orbiting X-ray telescope belonging to the Einstein X-ray Observatory; and the International Sun-Earth Explorer (ISEE). Barat et al. (1983) analyzed data from three of these spacecrafts, Prognoz 7, Venera 11, and Venera 12. They found an 8 second spin period for the neutron star as well as a potential QPO with a frequency of 43.5 Hz. As this was the first giant flare ever recorded astronomers had not been prepared for this type of stellar activity which may be the reason why only one QPO was detected from this source.

1.2.2 SGR 1806-20

This burster is located in the Galactic plane in the constellation Sagittarius. Its first flare was detected in January 1979 and it continued to emit over 100 more during the eighties, emitting fewer throughout the nineties. In 2004 it made a comeback by emitting the most energetic and recent giant flare ever recorded with an isotropic energy of $\sim (3 - 10) \times 10^{46}$ ergs (Israel et al. 2005). This burst was recorded by the Rossi X-ray Timing Explorer (RXTE) Proportional Counter Array (PCA) (Israel et al. 2005) and the Ramatay High Energy Solar Spectroscopic Imager (RHESSI) (Strohmayer & Watts 2005).

Analysis of the RXTE data (Israel et al. 2005) determined a short lived ~92.5 Hz X-ray QPO in the tail of the flare, detected $\approx 170-220$ seconds after the main peak. This neutron star's spin period is 7.56 s and the QPO seemed to be dependent on this rotational phase, only appearing during specific intervals of the period. This phase dependence implies that the QPO is occurring on a specific area of the neutron star. At later times, between $\approx 200-300$ seconds after the initial pulse, two additional QPOs were detected at ~18 and ~30 Hz. These oscillations were weaker than the first one and there was no conclusive evidence found for their phase dependence.

When the RHESSI data were analyzed by Watts and Strohmayer (2006) they also found a ~92.5 Hz QPO confirming the result found by the RXTE PCA. They found the signal was strongest between $\approx 150-260$ seconds after the main peak and it was at a rotational phase away from the main pulse just as it had been in the RXTE data. Additional oscillations were found at ~18, 26, and 30 Hz (this detection was much weaker). These low frequency QPOs were found earlier than 200 seconds after the main spike (a bit earlier than those found by Israel et al. 2005) and the two lowest frequencies were found at the same rotational phase as the 92.5 Hz oscillation. The 30 Hz QPO was too weak to be significant. One more QPO was found in this dataset at ~ 626.5 Hz, occurring before the 92.5 Hz oscillation between 50 and 200 seconds after the main flare. It was detected at a different rotational phase, much closer to the main peak, than all the other signals.

Once Strohmayer and Watts had analyzed the RHESSI data the RXTE PCA data became public. They re-analyzed the RXTE detections and confirmed the QPOs found by Israel et al. (2005) at ~18, 30 and 92.5 Hz (Strohmayer & Watts

2006). They were also able to confirm a rotational phase dependence for all three of these QPOs, which had not done by Israel et al. (2005). Extending their search to higher frequency ranges they found additional QPOs at $\sim$ 150 and 1840 Hz and two more oscillations with lower significances at $\sim$ 720 and 2384 Hz. The most exciting result from this analysis was the detection of QPOs at $\sim$ 26 and 625 Hz, two results observed in the RHESSI data which had not been found during the first RXTE analysis. The fact that both satellites were detecting oscillations at the same frequencies implied that these QPOs were really intrinsic to their source.

1.2.3 SGR 1900+14

This star is situated in the Galactic plane on the outskirts of a SNR (G42.8 $\pm$ 0.6) in the constellation Aquila, the Eagle (Feroci et al. 2001). It was not very active in its early years, bursting three times in 1979 (Mazets et al. 1979b) and then not again until 1992 (Kouveliotou et al. 1993), emitting another three bursts. On August 27th 1998 this SGR became much more exciting, producing the most luminous event ever detected outside our solar system at the time, with a peak source luminosity $\gtrsim 2 \times 10^{44}$ ergs s^{-1} (Hurley et al. 1999). The actual burst was intrinsically less powerful than that in SGR 0526-66, but because SGR 1900+14 is closer to Earth the flux was more intense. However it would only hold this record for another six years before SGR 1806-20 would burst, overpassing both hyperflares and becoming the most luminous SGR burst ever observed.

Hurley et al. (1999) detected this event, having the same initial hard peak of gamma rays followed by a softer decaying tail (lasting $\approx$ 300 s) as the March 5th event of SGR 0526-66. They discuss the detection of a rotational period of 5.16 s for the neutron star which was also found in the analysis of the BeppoSAX and Ulysses data from this flare (Feroci et al. 2001).

After Israel et al. (2005) had found QPOs in the hyperflare emitted by SGR 1806-20 Stroymayer and Watts (2005) decided to look for similar behavior in the data from SGR 1900+14. They used signals from the RXTE PCA and discovered QPOs at $\sim$ 28 (weakest detection), 53.5, 84, and 155.1 Hz. They also found that each oscillation was at the same rotational phase and not centered on a peak, which had already been shown for the QPOs from SGR 1806-20 (Israel et al. 2005). The similarity between the QPOs for SGR 1900+14 and SGR 1806-20 gives more evidence that these signals are associated with the source, which is promising for future understanding of these interesting astrophysical objects. See Table (1−1) for a summary of the observed frequencies from all three hyperflares.

1.2.4 SGR 1801-23

In the summer of 1997 when SGR 1806-20 was extremely active two bursts were observed near this source that were inconsistent with its behavior. This turned out to be a new burster, SGR 1801-23. Four separate instruments detected these flares; BATSE aboard Compton Gamma Ray Observatory (CGRO) (Meegan et al. 1996), Konus-A aboard the Kosmos spacecraft (Aptekar et al. 1995), and the gamma-ray burst (GRB) experiment aboard Ulysses (Hurley et al. 1992). Cline et al. (2000) attempted to locate the burster by analyzing potential SNRs that it may be associated with. Unfortunately, due to minimal detections from this SGR, there is currently not enough information to learn much more about it. Hopefully it will

Table 1–1: Approximate frequency results from all three hyperflares where the numbers beside the satellites represent the papers revealing these QPOs: [1] Watts & Strohmayer (2006); [2] Strohmayer & Watts (2006); [3] Israel et al. (2005); [4] Barat et al. (1983); [5] Strohmayer & Watts (2005). Notice the similarities between some of the observed frequencies from different sources, implying that the same phenomenon is powering these flares.

Frequency (Hz)	SGR	Satellite
18	1806-20	RHESSI [1] & RXTE [2, 3]
26	1806-20	RHESSI [1] & RXTE [2]
28	1900+14	RXTE [5]
30	1806-20	RXTE [2, 3] & RHESSI (weak) [1]
44	0526-66	Prognoz 7, Venera 11 & 12 [4]
54	1900+14	RXTE [5]
84	1900+14	RXTE [5]
93	1806-20	RHESSI [1] & RXTE [2, 3]
150	1806-20	RXTE [2]
155	1900+14	RXTE [5]
625	1806-20	RHESSI [1] & RXTE [2]
720	1806-20	RXTE (weak) [2]
1837	1806-20	RXTE [2]
2384	1806-20	RXTE (weak) [2]

become active again in the future giving us more insight into these new and exciting sources.

1.2.5 SGR 1627-41

SGR 1627-41, our newest SGR, was first detected in 1998 (Kouveliotou et al. 1998). It is located in a SNR near the Galactic plane. In the summer of 1998, 99 bursts were detected from this source by the Burst and Transient Source Experiment (BATSE) (Woods et al. 1999). An estimated neutron star spin period of 6.4 s was calculated from these bursts (lasting between 25 ms and 1.8 s). No QPOs have been observed in this source, and therefore we will not consider it any further in this dissertation.

1.3 History of Theoretical Work on QPOs Produced by SGRs

1.3.1 Seismic Vibration Models

Early considerations of neutron star oscillations laid out the ground work for future research on SGRs. One of these papers (McDermott et al. 1988) described numerous types of nonradial oscillations that could potentially occur in neutron stars. Throughout this work rotation, general relativity, and magnetic field effects were ignored and it was assumed that the crustal motion had no dependence on the motion of the fluid core.

Stellar oscillations can be classified into two main types, spheroidal and toroidal modes. There are several subcategories within these modes. Toroidal oscillations are the most interesting and most likely candidates for SGR giant flares. They can be described as normal modes of shear waves in the solid neutron star crust. They are divergence free and have no radial components. In order to study these oscillations McDermott et al. (1988) derived the perturbed wave equation caused by the shearing of the elastic crust and solved for the eigenfunctions.

For the numerical calculations McDermott et al. (1988) used four neutron star models. In the short wavelength limit an analytic estimate for the dispersion relation was calculated, allowing for numerical approximations of these oscillation periods to be made. By using the spherical harmonics ℓ and n to classify the torsional modes, where ℓ is the spherical harmonic index and n represents the number of nodes in the radial eigenfunction, the fundamental period (n=0, ℓ=2) was found to be $\sim$20 ms for all four models. Other results showed that the eigenfunctions and periods of the overtones ($n > 0$) were not dependent on ℓ. See Table (1–2) for a summary of these periods. These numerical solutions, for the fundamental and overtone periods, were in good agreement with the analytic calculations given by Hansen & Cioffi (1980) where the fundamental period is given by,

$$P_{n=0} \approx \frac{60 \text{ ms}}{[\ell(\ell+1)]^{1/2}} R_6 \tag{1.1}$$

and the overtone period is,

$$P_{n>0} \approx \frac{2 \text{ ms}}{n} \frac{\Delta r}{1 \text{ km}} \tag{1.2}$$

where $R_6 = R/10^6$ cm and Δr is the crust thickness. These period calculations are what we would expect since the lowest order modes can be estimated by the time it takes a shear wave to travel around the neutron star ($P_{n=0} \approx R/v_s$), whereas the higher order modes can be estimated by the time it takes for a shear wave to travel vertically through the crust divided by the number of radial nodes ($P_{n>0} \approx H/nv_s$), where v_s is the shear speed and H is the scaleheight. Additional numerical results concluded that the ratio of overtone to fundamental periods could give an estimate for the thickness of the neutron star crust, also agreeing with the equations (1.1) and (1.2). This implies that the observation of these modes could potentially lead to a greater understanding of the structure of neutron stars.

The idea of starquakes has been around since long before the magnetar model existed and also before many SGR bursts had been observed. The theory of starquakes as the cause of gamma ray bursts was considered by Blaes et al. (1989). A

Table 1–2: Period results from McDermott et al.'s (1988) neutron star models. The torsional modes are denoted by ${}_{\ell}t_{n}$, where ℓ is the spherical harmonic index and n represents the radial node number. The bracketed numbers refer to the different models where; [1] is the fiducial model ($M = 0.503 M_{\odot}$, $R = 10.1$ km, and $\rho_{central} = 9.44 \times 10^{14}$ gcm^{-3}, [2] is NS05T7 ($M = 0.503 M_{\odot}$, $R = 9.839$ km, and $\rho_{central} = 9.44 \times 10^{14}$ gcm^{-3}), [3] is NS05T8 ($M = 0.503 M_{\odot}$, $R = 9.785$ km and $\rho_{central} = 9.44 \times 10^{14}$ gcm^{-3}, and [4] is NS13T8 ($M = 1.326 M_{\odot}$, $R = 7.853$ km, and $\rho_{central} = 3.63 \times 10^{15}$ gcm^{-3}.

Mode	Period (ms) [1]	Period (ms) [2]	Period (ms) [3]	Period (ms) [4]
${}_{1}t_{1}$	1.749	1.885	1.795	0.3512
${}_{1}t_{2}$	1.015	1.097	1.050	0.2079
${}_{1}t_{3}$	0.8315	0.8199	0.7547	0.1457
${}_{1}t_{4}$	0.6689	0.7027	0.6382	0.1192
${}_{2}t_{0}$	19.06	18.59	18.54	17.32
${}_{2}t_{1}$	1.742	1.877	1.788	0.3512
${}_{2}t_{2}$	1.014	1.096	1.049	0.2079
${}_{2}t_{3}$	0.8307	0.8190	0.7539	0.1457
${}_{2}t_{4}$	0.6685	0.7022	0.6378	0.1192

starquake is believed to occur when the neutron star crust is fractured and elastic energy is released. This energy excites the surface magnetic field, producing an induced electric field which then ejects energy in the form of gamma rays. Blaes et al. (1989) concluded that the elastic energy stored in neutron star crusts was large enough to produce the required amount of energy observed for various gamma ray bursts, such as the March 5th event which had been detected by this time. However, they also believed that the energy may not have been enough to produce the multiple bursts that had been observed for various gamma ray bursts, specifically SGR 0526-66. At the time of this research magnetars were not a possible option, as they had not been thought up yet. Therefore the magnetic energy estimate for these calculations was much lower than our values today since magnetic fields on the order of 10^{12} G were being used as opposed to the now known field strengths of $\sim 10^{14} - 10^{15}$ G.

Once the magnetar model was proposed (Duncan & Thompson 1992, Thompson & Duncan 1995) and SGRs were defined as a distinct set of objects, research advanced dramatically. Duncan (1998) proposed that SGRs undergo frequent starquakes, produced by global seismic fractures of the crust which are powered by extremely strong magnetic fields. Neutron stars are the most likely candidates for starquakes because their thin crust requires less energy to produce observable shear modes than a completely solid object. In addition to the shear modulus, isotropic magnetic pressure is included in the theory and the assumption is that low order toroidal modes should be excited by these crustquakes. The suggestion is that a global crust fracture occurred for the March 5th event, creating oscillation modes that emitted radiation with observable frequencies. An analytic estimate of the toroidal frequencies was calculated and compared to that found for SGR 0526-66, classifying it as the fundamental toroidal mode ($\ell = 2, n = 0$). Due to the restricted data for this SGR only one period could be compared to the theory as it was the only one detected.

After three giant flares had been detected theoretical models progressed even further. Piro (2005) used simplified magnetic field and crustal geometries to calculate the eigenfrequencies and eigenfunctions expected for torsional oscillations from SGRs. He considered how the magnetic field and observed frequencies were related, as well as how the modes depend on the properties of neutron stars. His work will be described in full in Chapter 2.

Following Piro's work, there have been numerous attempts to modify and improve these theoretical models. General Relativistic effects and elasticity were considered by Samuelsson & Andersson (2007), although they used a zero temperature model and did not include magnetic field effects. They simulated many different models with varying core masses and radii, finding mode frequencies comparable to those observed for SGR 1806-20 and SGR 1900+14. Their results can be seen in Table (1–3) and it should be noted that the lowest observed SGR 1806-20 frequencies, 18 and 26 Hz do not fit into these models.

Table 1–3: Mode identification for the observed QPO frequencies of SGR 1806-20 and SGR 1900+14 (Samuelsson & Andersson 2007).

SGR 1806-20		SGR 1900+14	
Frequency (Hz)	Mode	Frequency (Hz)	Mode
29	${}_0t_2$	28 ± 0.5	${}_0t_2$
92.7 ± 0.1	${}_0t_6$	53.5 ± 0.5	${}_0t_4$
150.3	${}_0t_{10}$	84	${}_0t_6$
626.46 ± 0.02	${}_1t_\ell$	155.1 ± 0.2	${}_0t_{11}$

None of the work described above has included the effect of the coupling between the solid crust and fluid core by the magnetic field. The most recent papers looking into this problem are; Glampedakis et al. (2006), Lee (2007), and Sotani et al. (2006 & 2007), following previous attempts by Carroll et al. (1986) and Messios et al. (2001). Glampedakis et al. (2006) claimed that in order to have an accurate picture of these oscillations one must consider the global system of the coupled crust and core. The reason for this is that any time the crust is deformed, the magnetic field will also be disrupted, causing Alfvén waves to travel into the core where they can be reflected by the crust once they have reached the other side. In order to calculate the complete set of coupled magneto-elastic modes they used the same simplified plane parallel geometry as Piro (2005), adding the core into the calculations. This leads to very interesting results. The coupled system has a set of modes, and within this set most of the frequencies for the pure crustal modes are found as well as lower frequency modes, potentially comparable to the modes observed from SGR 1806-20 which could not be explained by the uncoupled system! In order to understand why the majority of the modes observed are similar to the pure crust modes, Glampedakis et al. (2006) calculate the total energy ratios between the crust and core. The modes maximizing this energy ratio should be the easiest to excite and thus those detected. The result is that the crustal frequencies are more energetically favorable explaining why we mostly observe these modes as opposed the core-Alfvén modes.

After the release of Glampedakis et al.'s paper Sotani et al. (2006 & 2007) studied the crust-core coupling in relativistic neutron stars with dipole magnetic fields, following previous work by Messios et al. (2001). To understand the combined crustal torsional modes and global Alfvén modes two special cases (ie. toy models) are considered before the realistic model is calculated. The first is for a completely fluid neutron star with no crust at all and therefore only pure Alfvén modes can exist. In the second case crusts of varying thicknesses are studied in order to see how the inclusion of a crust affects the Alfvén modes. For a completely solid star only crustal modes are present as would be expected. However, as soon as any amount of fluid is introduced global Alfvén modes arise. At this point both modes are present, the Alfvén modes penetrate the crust while the torsional crustal modes enter the core. As the magnetic field increases and the crust thickness decreases

Alfvén modes become more dominant throughout the star. Therefore, for realistic neutron star models with crust thicknesses varying between 3 and 12% depending on the equation of state and mass of the star, Sotani et al. (2006 & 2007) conclude that global Alfvén modes are dominant over the torsional crustal modes and these are the oscillations we observe. They also claim that global Alfvén modes are not affected at all in the presence of a realistic size neutron star crust for $B > 4 \times 10^{15}$ G and that these modes can explain all the observed frequencies, including those very close together that cannot be explained by pure crustal modes (ie. the 26 and 29 Hz QPOs found from SGR 1806-20). The reason for this is that the Alfvén mode overtone frequencies are non-degenerate for different values of ℓ. See Table (1–4) for a comparison between the computed global Alfvén modes and the frequency results for SGR 1806-20 and SGR 1900+14. Another benefit to this theory is that it puts an upper limit on the magnetic field strengths for these SGRs, finding $B_{max} \approx 8 \times 10^{15}$ G for SGR 1806-20 and $B_{max} \approx 12 \times 10^{15}$ G for SGR 1900+14.

Table 1–4: Alfvén mode identification for the observed QPO frequencies of SGR 1806-20 and SGR 1900+14, denoted by ${}_{\ell}a_n$. (Sotani et al. 2006).

SGR 1806-20		SGR 1900+14	
Frequency (Hz)	Mode	Frequency (Hz)	Mode
18	${}_2a_0$	28	${}_2a_0$
26	${}_4a_0$	–	–
29	${}_5a_0$	54	${}_7a_0$
92.5	${}_5a_2$	84	${}_3a_1$
150	${}_5a_4$	155	${}_6a_2$
626.5	${}_4a_{25}$	–	–
720	${}_4a_{29}$	–	–
1837	${}_2a_{83}$	–	–
2384	${}_2a_{108}$	–	–

Lee (2007) also studied the effects of a coupled ocean, crust, and core system with a dipole magnetic field. Their analysis was simplified by assuming a non-magnetic core and ignoring the effects of general relativity. In addition to studying toroidal modes they expanded their work to include spheroidal modes, magnetic modes in the crust and ocean, and the effects of slow rotation which ignored possible rotational deformations. Spherical geometry was employed, a more realistic model than the cylindrical geometry used by Carroll et al. (1986). Other improvements over Carroll et al.'s work was the inclusion of the fluid core and realistic magnetar field strengths, where Carroll et al. had only included the ocean/crust system and magnetic field strengths of $B \approx 10^{12}$ G.

Lee (2007) did not attempt to compare their findings to observed oscillations, although they did mention that for frequencies less than 100 Hz it is extremely likely that these are fundamental torsional modes with low ℓ's, whereas for frequencies greater then 100 Hz the evidence is not concrete. Therefore claiming if we do not know anything else about the observed neutron stars we can not a priori classify the toroidal modes with these frequencies, other possible modes must also be considered. An example of this is for frequencies between 100 and 1000 Hz. In this situation the modes could be fundamental toroidal modes with high ℓ values, toroidal modes with $n \geq 1$ and low ℓ values, overtone spheroidal modes with low ℓ values, or crust/core interfacial modes with $n = 2$. Additional modes for the observed QPOs with extremely high frequencies, such as 1835 and 2384 Hz found from SGR 1806-20, must be considered as well. Therefore concluding that pure toroidal modes may be too simplistic an analysis for the observed QPOs.

1.3.2 Different Models

One of the alternate ideas to neutron star torsional oscillations is the theory that magnetars are actually strange stars. These stars are composed almost completely of stable strange quark matter and there are two possibilities for their structure. The first is a bare strange quark star where the star is made of extremely dense quark fluid. Obviously this model could not house shear modes but the second type of strange star, one with a solid crust, could. There exist two different crustal theories. One is in which an electric field suspends the crust above the quark liquid. The composition of this crust is similar to that of a neutron star although it is thinner, only going as deep as neutron drip. The other kind of crust is one where strange quark nuggets exist in a background of uniform electrons; again this is much thinner than a neutron star crust.

Following the approach used by Piro (2005), Watts and Reddy (2006) consider torsional oscillations for both types of crustal compositions and compare their results to the observed QPOs of SGRs. For the nuclear crust model they find the lowest possible fundamental frequency for a magnetic field strength of $B > 10^{14}$ G to be 34 Hz, thus ruling out the possibility of the strange star model revealing the lowest observed QPO frequencies. While for the first overtone with the same magnetic field they find a lower limit frequency of $\sim$ 1660 Hz, much higher than the observed 625 Hz. The results for the nugget crust are no more promising; the minimum frequency for all parameters considered is 1.5 Hz, while the maximum is 20.7 Hz. These values could potentially agree with some of the observations although it would be difficult to find mode scalings with ℓ. For the higher frequency calculations a similar conclusion to the nuclear crust case was reached; even the minimum overtone frequencies were too high where for $B > 10^{14}$ G, $\nu_{min} \approx 920$ Hz. These results imply that if we are in fact witnessing torsional shear QPOs from SGRs than the strange star hypothesis is unlikely for these objects.

A recent paper by Levin (2006a) disagrees with the torsional shear mode analysis for SGRs claiming it contradicts the magnetar model. In his paper he includes the influence of the coupled crust/core system and argues that the crustal modes decay much too quickly, because of Alfvén wave propagation into the core, and can therefore not be observed as QPOs. He begins his work by considering a toy model of the core on its own and solves for the eigenmodes. The result is a continuous spectrum of magnetohydrodynamic (MHD) modes. He proceeds to add the crust into the model showing that any movement of the crustal modes will be coupled to the continuum of core modes. Claiming that these combined global modes will decay on the order of one second, much shorter than the observed $\sim$ 100 s QPOs, as energy rapidly transfers from the crust to the core. He concludes that mechanical fracturing of the crust cannot be the mechanism behind these magnetar flares and suggests two potential candidates for these bursts. The first possibility is a different magnetic field configuration, either it is dominant in the crust or its poloidal component is incoherent. The second option is that these QPOs originate in the neutron star's magnetosphere as opposed to its crust.

Levin (2006b) has a follow-up paper where he creates a more complicated toy model to better understand the occurrence of oscillations in magnetar crusts when a continuum of Alfvén modes is present in the core. They create 10^4 oscillators to simulate the continuum of MHD modes in the core. Next they attach one single oscillator to this continuum and mimic the crustal motion by releasing it. In doing this they find that the energy drains into the core very quickly, confirming their previous predictions (Levin 2006a). Once the crust has transferred a large portion of its energy to the core it stabilizes and produces observable QPOs, explained by the turning points and edges of the Alfvén continuum. They claim that this model produces the 18 Hz QPO observed from SGR 1806-20 and potentially some of the other detected frequencies as well. In this paper they also refute previous calculations of crust/core coupled torsional modes (Glampedakis et al. 2006 and Sotani et al. 2006b), arguing that the mis-use of symmetry in each case leads to the incorrect assumption of a discrete set of Alfvén modes.

Strohmayer and Watts (2007), on the other hand, agree with the work done by Glampedakis et al. (2006) and Sotani et al. (2006) and discredit Levin's (2006a) work. Their first criticism is that the continuous spectrum is a result of the simplified geometry and would not hold in a more realistic system. They also point out that the model is not complete, including only one top plate as the sheared crust. A full slab core model should have two plates representing the crust, one on the top and one on the bottom which would definitely change the results of the calculations. This would also be true for the more complex toy model (Levin 2006b), where there should be a bottom crust oscillator as well as the top one. Therefore, more work will have to be done on this model before it gains popularity over the global seismic torsional oscillation model.

There have been two other suggestions on the theory of SGR QPOs which were summarized in Strohmayer and Watts (2007) paper. One of these suggestions stems from the fact that high frequency QPOs have been observed in several accreting neutron star binary systems (van der Klis 2006). Recently, when a debris disk was found around an AXP (Wang et al. 2006) it led to the idea that debris disks surrounding magnetars could perhaps exhibit similar behavior as accretion disks around regular neutron stars and could therefore produce the observed SGR QPOs. Strohmayer and Watts (2007) claim that this idea is weak for a few reasons. First of all there has been no proof of a debris disk surrounding SGRs. Secondly, none of the binary system QPOs have had similar sets of frequencies to any of the observed magnetar flares nor have they exhibited a dependence on rotational phase. The final and strongest reason Strohmayer and Watts (2007) discredit this theory is that the observed binary system QPOs are due to the proximity of the inner accretion disks to their neutron stars. The observed magnetar debris disk is much farther away from its star and would therefore not exhibit high frequency QPOs. At the present time Strohmayer and Watts (2007) conclude that this theory seems rather unlikely.

The second alternate theory to seismic vibrations of the crust is that Alfvén waves in the magnetosphere produce the observed QPOs, one of the possibilities mentioned by Levin (2006a). It has been suggested that the inner corona is capable of producing high frequency QPOs while the outer corona could potentially create the lower frequency ones. However due to reduced emission around the outer corona it may be difficult for the observed frequencies to be reached. More work is needed on this theory before it can be credited as a viable option or completely discredited.

1.4 Outline

We begin in Chapter 2 by giving an in depth description of the shear wave analysis for hyperflares from SGRs, comparing our results to Piro's (2005) throughout. We will explain the theories and produce simplified theoretical models of the modes of these neutron stars, showing the relationship between magnetic field strength and observed frequency. In Chapter 3, we will broaden the analysis by producing a toy model to see how different field geometries affect the QPOs. We will conclude our work in Chapter 4 and give suggestions for future research on these new and exciting objects.

CHAPTER 2
Torsional Shear Modes from SGRs

In this chapter we will consider a plane-parallel model of the neutron star crust. This model is similar to that calculated by Piro (2005), and we compare our results to his where possible. Despite being a rather simplified model it has been extremely useful in broadening our knowledge on torsional oscillations in neutron star crusts. We will attempt to complicate the model by changing the field geometry in Chapter 3 in the hopes that this will give more insight into the QPOs produced by SGRs. In this chapter we begin by describing the key equations for studying the torsional modes (section 2.1). We then make some analytic estimates on how the equations will behave (section 2.2) and end the chapter by discussing our numerical results (section 2.3).

2.1 The Main Equations

Our simplified model uses a plane-parallel geometry where z is the radial coordinate. We choose a mass $M = 1.4\ M_{\odot}$ and a radius $R = 1.2 \times 10^6$ cm which gives us a gravitational acceleration of $g = GM/R^2 \approx 1.3 \times 10^{14}$ cm s^{-2}, where G is the gravitational constant defined as $G \equiv 6.67 \times 10^{-8}$ cm^{3}g^{-1}s^{-2}. We also choose a constant magnetic field $\vec{B} = B\hat{\mathbf{z}}$, and a Lagrangian displacement $\vec{\xi} = \xi_x\hat{\mathbf{x}} + \xi_y\hat{\mathbf{y}}$. Our model is isothermal with a temperature $T = 5.1 \times 10^8$ K. Shear waves can only exist in solids and therefore will not be present in the fluid ocean or core. These waves are incompressible ($\vec{\nabla} \cdot \vec{\xi} = 0$), axisymmetric, and have no vertical displacement.

In order to proceed, we must determine the equation for the shear modulus in neutron star crusts. The shear modulus describes how rigid the solid is. It is defined by the ratio of shear stress to shear strain of the material. The shear stress for toroidal modes arises from Coulomb forces between the ions in the neutron star crust described by

$$\frac{F}{a^2} \approx \frac{1}{a^2}\frac{(Ze)^2}{a^2}\frac{\delta x}{a}, \tag{2.1}$$

while the shear strain comes from the displacement of the ions from equilibrium given by $\delta x/a$. See Figure (2–1) for a simple diagram of this system. Here Z is the atomic number of the ions, a is the average inter-ion spacing, e is the electronic charge, and δx is the infinitesimal displacement of the ions. This implies that a simple two dimensional estimate of the shear modulus is

$$\mu \approx \frac{(Ze)^2}{a^4} \propto {n_i}^{4/3}, \tag{2.2}$$

where n_i is the number density of the ions and $4\pi n_i a^3/3 = 1$. Complications arise due to the anisotropy of the neutron star crust and numerical calculations must be employed to obtain a better solution for the shear modulus. We use the one calculated by Strohmayer et al. (1991) where they model the neutron star crust as a Coulomb solid and assume that it is a perfect body-centered-cubic (bcc) crystal. This solid crust consists of positively charged ions in a uniform negatively charged background. By averaging over all possible shear wave directions they solve for an effective shear modulus given by

$$\mu = \frac{0.1194}{1 + 0.595(173/\Gamma)^2}\frac{n_i(Ze)^2}{a}, \tag{2.3}$$

where Γ is the ratio of Coulomb to thermal energy $((Ze)^2/ak_bT)$.

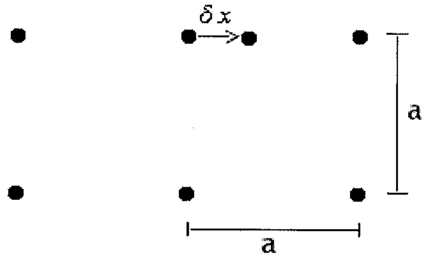

Figure 2–1: Depiction of the infinitesimal displacement of the ions in a Coulomb solid.

In a three dimensional solid undergoing small deformations the strain is described as a symmetric tensor as opposed to the two dimensional $\delta x/a$. This shear strain tensor is given by

$$u_{ij} = \frac{1}{2}\left(\frac{\partial \xi_i}{\partial x_j} + \frac{\partial \xi_j}{\partial x_i}\right) = u_{ji}, \tag{2.4}$$

which for toroidal displacements of the form $\vec{\xi} = \xi_x \hat{\mathrm{x}} + \xi_y \hat{\mathrm{y}}$ gives us a shear stress tensor defined by $\delta\sigma_{ij} = 2\mu u_{ij}$ (McDermott et al. 1988).

We are now in a position to write the equation of motion for the ions including shear and magnetic forces:

$$\rho\frac{\partial^2 \vec{\xi}}{\partial t^2} = \vec{\nabla} \cdot \delta\vec{\sigma} + \frac{1}{c}(\delta\vec{j} \times \vec{B}). \tag{2.5}$$

By assuming a periodic time dependence $\vec{\xi} \propto e^{i\omega t}$, where ω is the frequency, and writing (2.5) in component form, the equation of motion simplifies to

$$-\rho\omega^2\xi_i = \frac{\partial}{\partial x_j}\delta\sigma_{ij} + \frac{1}{c}(\delta\vec{j} \times \vec{B})_i, \tag{2.6}$$

where $\delta\vec{j}$ is the perturbed current density due to the shaking of the crust. We can solve for $\delta\vec{j}$ as a function of $\vec{\xi}$ using three equations (Blaes et al. 1989). First we treat the crust as a perfect electrical conductor. This is a good approximation since the period time-scale for these modes is much shorter than the ohmic dissipation time-scale (Blaes et al. 1989). The perturbed electric field is given by

$$\delta\vec{E} = -\frac{1}{c}\frac{\partial\vec{\xi}}{\partial t} \times \vec{B}. \tag{2.7}$$

We then use Faraday's Law

$$\vec{\nabla} \times \delta\vec{E} = -\frac{1}{c}\frac{\partial(\delta\vec{B})}{\partial t}, \tag{2.8}$$

and Ampère's law

$$\vec{\nabla} \times \delta\vec{B} = \frac{4\pi}{c}\delta\vec{j} + \frac{1}{c}\frac{\partial(\delta\vec{E})}{\partial t}, \tag{2.9}$$

for the perturbed fields. In order to eliminate $\delta\vec{E}$ from these equations we simply plug (2.7) into equations (2.8) and (2.9). We can then solve for $\delta\vec{B}$ in terms of $\vec{\xi}$ and $\vec{B}$ using (2.8), and we can then get $\delta\vec{j}$ in terms of $\delta\vec{B}$, $\vec{\xi}$, and $\vec{B}$ using (2.9) and the oscillatory time dependence of $\vec{\xi}$. The resultant perturbed magnetic field and current density equations are given by

$$\delta\vec{B} = \vec{\nabla} \times (\vec{\xi} \times \vec{B}), \tag{2.10}$$

and

$$\delta\vec{j} = \frac{c}{4\pi}\Big(\vec{\nabla} \times \delta\vec{B} - \frac{\omega^2}{c^2}\vec{\xi} \times \vec{B}\Big). \tag{2.11}$$

Combining equations (2.6), (2.10), and (2.11) gives us the full wave equation for these modes

$$-\rho\omega^2\vec{\xi} = \mu\nabla_\perp^2\vec{\xi} + \frac{\partial}{\partial z}\left(\mu\frac{\partial\vec{\xi}}{\partial z}\right) + \frac{B^2}{4\pi}\left(\frac{\partial^2\vec{\xi}}{\partial z^2} + \frac{\omega^2}{c^2}\vec{\xi}\right), \tag{2.12}$$

where $\nabla_\perp^2 = \partial^2/\partial x^2 + \partial^2/\partial y^2$. It should be noted that Piro (2005) used $\nabla_\perp^2\vec{\xi} = -\ell(\ell+1)\vec{\xi}/R^2$, whereas we will use the correct scaling of $\nabla_\perp^2\vec{\xi} = -(\ell+2)(\ell-1)\vec{\xi}/R^2$ (Watts & Reddy 2006, Samuelsson & Andersson 2007) for our calculations.

2.2 Simplified Analysis

We now make a few approximations in order to estimate the dispersion relation for toroidal modes. We assume $\vec{\xi} \propto e^{i(k_x x + k_y y + k_z z)}e^{i\omega t}$ and that μ is constant. Equation (2.12) becomes

$$\omega^2 = v_s^2(k_z^2 + k_\perp^2) + v_a^2\left(k_z^2 + \frac{\omega^2}{c^2}\right), \tag{2.13}$$

where the transverse wavenumbers $(k_x^2 + k_y^2)$ are represented by $k_\perp^2$, k_z is the vertical wavenumber, $v_s = (\mu/\rho)^{1/2}$ is the speed of shear waves through the crust, and $v_A = B/(4\pi\rho)^{1/2}$ is the Alfvén wave speed. The transverse wavelength scales with the horizontal radius of the star $k_\perp \propto 1/R$, while the vertical wavelength scales with the vertical depth of the crust $k_z \propto 1/H$, where $H = P/\rho g$ is the pressure scaleheight.

We will consider two specific cases, one for the modes traveling radially around the star ($n = 0$), and the second for the overtone modes ($n > 0$) traveling vertically through the crust. For the first case $k_z \approx 0$ and equation (2.13) becomes $\omega^2 = v_s^2k_\perp^2/(1 - v_A^2/c^2)$. The term v_A^2/c^2 is important in the limit $v_A \rightarrow c$. This limit tells us that $B^2/4\pi\rho c^2 = 1$ which we use to solve for the critical density $\rho_{crit} = B^2/4\pi c^2 \approx 10^7 - 10^8$ g cm^{-3} for magnetar field strengths. Therefore as long as $\rho > \rho_{crit}$, which it is throughout the crust, $v_a < c$ and we can drop this term from our expression, giving a dispersion relation $\omega^2 \approx v_s^2 k_\perp^2$ for the $n = 0$ modes. Our numerical calculations confirm that neglecting this term does not affect our frequency results.

In the second case k_z^2 is much larger than $k_\perp^2$ as long as ℓ remains relatively small. The dispersion relation for this situation is given by $\omega^2 = (v_s^2 + v_A^2)k_z^2$ where we have dropped the v_a^2/c^2 term again. These two simple estimates show that the lowest radial-order mode depends on the spherical harmonic index ℓ and does not depend on B using our simplified field geometry, whereas the higher radial-order modes are proportional to B and independent of ℓ.

One final analytic calculation made by Piro (2005) was to estimate the observed fundamental frequencies of these modes. He first calculated the shear modulus at the base of the crust

$$\mu_{base} = 1.2 \times 10^{30} \text{ ergs cm}^{-3}\ \rho_{14}^{4/3}\left(\frac{Z}{38}\right)^2\left(\frac{302}{A}\right)^{4/3}\left(\frac{1-Y_n}{0.25}\right)^{4/3}, \tag{2.14}$$

where A is the atomic mass number, Y_n is the fraction of neutrons, and $\rho_{14} \equiv \rho/10^{14}$ g cm^{-3}. Our shear modulus at the base agrees with Piro's, where we find $\mu = 1.3 \times 10^{30}$ ergs cm^{-3}, $\rho = 1 \times 10^{14}$ g cm^{-3}, $Z = 38$, $A = 303$, and $Y_n = 0.74$. Once Piro (2005) had calculated equation (2.14) he used the estimated $n = 0$ dispersion relation ($\omega^2 = v_s^2 k_\perp^2 = \mu_{base}\ell(\ell+1)/\rho_{base}R^2$) and the effect of gravitational redshifting $(1 - 2GM/Rc^2)^{-1/2}$ to obtain the solution

$$\begin{aligned} \nu_{obs}\Big|_{n=0} = \frac{\omega_{obs}}{2\pi}\Big|_{n=0} &= 28.8 \text{ Hz}\ \rho_{14}^{1/6}\left(\frac{Z}{38}\right)\left(\frac{302}{A}\right)^{2/3}\left(\frac{1-Y_n}{0.25}\right)^{2/3} \\ &\times \left[\frac{\ell(\ell+1)}{6}\right]^{1/2} R_{12}^{-1}\left(1.53 - 0.53\frac{M_{1.4}}{R_{12}}\right)^{1/2}, \end{aligned} \tag{2.15}$$

where $M_{1.4} \equiv M/1.4M_{\odot}$ and $R_{12} \equiv R/12$ km. Using our values at the crust base in the above equation we find a fundamental frequency of $\nu_{obs} = 24.6$ Hz for $\ell = 2$ and $n = 0$, where we have replaced the $\ell(\ell+1)$ scaling with the corrected $(\ell+2)(\ell-1)$ value.

2.3 Numerical Results

2.3.1 Neutron Star Structure

The neutron star is made up of layers as mentioned in Chapter 1. The layers of interest for our model are the inner and outer crust and the fluid ocean. The inner crust contains nuclei with very high neutron numbers, electrons, and free neutrons. The density in this region ranges from $\rho_{drip} \approx 4 \times 10^{11}$ g cm^{-3} at the boundary between inner and outer crust and increases to $\rho_{c/c} \approx 1 \times 10^{14}$ g cm^{-3} at the crust/core interface. The transition from outer to inner crust (ρ_{drip}) occurs when neutron drip begins. At this point the neutron to proton ratio increases dramatically with increasing density and the nuclei emit free neutrons. By the time $\rho \geq 6 \times 10^{12}$ g cm^{-3} (Cumming et al. 2004) the pressure from these non-relativistic, degenerate neutrons completely dominates over the electron pressure. The fermi energy is $E_{f,n} = 15$ MeV $\rho_{14}^{2/3} Y_n^{2/3} (f/0.5)$ where f is a factor included to represent the neutron-neutron interactions. The neutron pressure is $P_n = (2/5) n_n E_{f,n} = 6.0 \times 10^{32}$ ergs cm$^{-3} \rho_{14}^{5/3} Y_n^{5/3} (f/0.5)$, where $n_n = \rho Y_n / m_p$ is the neutron number density and m_p is the proton mass.

The outer crust consists of heavy nuclei in a Coulomb lattice surrounded by relativistic, degenerate electrons. The top of the crust is found at the point where melting begins, defined by Piro (2005) and Farouki & Hamaguchi (1993) to be at

$$\Gamma = \frac{Ze^2}{k_B T}\left(\frac{4\pi}{3}\right)^{1/3}\left(\frac{\rho}{Am_p}\right)^{1/3} \approx 173. \tag{2.16}$$

We can use this to estimate the density at the top of the crust

$$\rho_{top} = 2.3 \times 10^9 \text{ g cm}^{-3} \left(\frac{T_8}{3}\right)^3 \left(\frac{26}{Z}\right)^6 \left(\frac{A}{56}\right). \tag{2.17}$$

The dominant pressure in this region ($\rho \leq 6 \times 10^{12}$ g cm^{-3}) comes from the relativistic, degenerate electrons. Their fermi energy is given by $E_{f,e} = 51$ MeV $\rho_{12}^{1/3} Y_e^{1/3}$ and their pressure is $P_e = (1/4) n_e E_{f,e} = 1.2 \times 10^{31}$ ergs cm$^{-3} \rho_{12}^{4/3} Y_e^{4/3}$, where $n_e = \rho Y_e / m_p$ is the electron number density, $\rho_{12} \equiv \rho / 10^{12}$ g cm^{-3}, and Y_e is the number fraction of electrons.

The third and final neutron star region we consider is the fluid ocean. We use a density range from $\rho = 3.5 \times 10^7$ g cm^{-3} to $\rho = 2.3 \times 10^9$ g cm^{-3} and set the composition to iron ($Z = 26, A = 56$). Since electrons become fully relativistic at $\rho \approx 10^7$ g cm^{-3} the pressure is still dominated by relativistic, degenerate electrons throughout the ocean.

We use the cold dense matter models of Haensel & Pichon (1994) for densities throughout the outer crust ($\rho < 4 \times 10^{11}$ g cm^{-3}) and Douchin & Haensel (2001) for densities throughout the inner crust ($\rho > 4 \times 10^{11}$ g cm^{-3}). We also use the models of Mackie and Baym (1977) to calculate the f factor arising in the neutron pressure. Using the above three models we calculate the atomic number Z, the neutron fraction Y_n, and the electron fraction Y_e as a function of density throughout the neutron star crust and ocean (Figure 2–2).

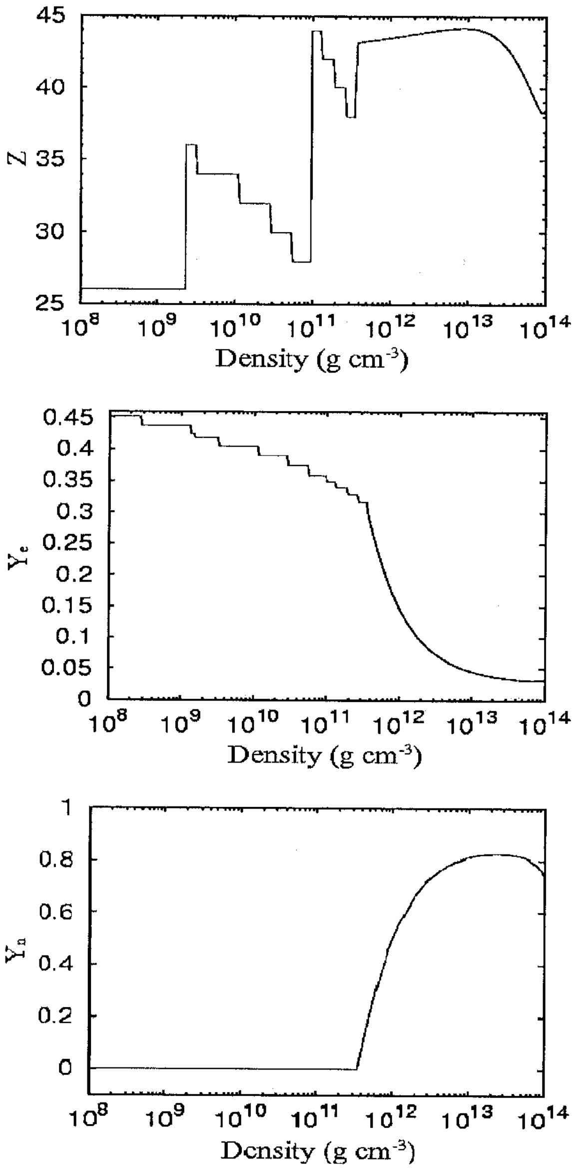

Figure 2–2: Atomic number Z, neutron fraction Y_n, and electron fraction Y_e versus density ρ throughout the neutron star crust and ocean. Note how quickly Y_e decreases and Y_n increases after neutron drip ($\rho_{drip} \approx 4 \times 10^{11}$ g cm^{-3}).

2.3.2 Numerical Procedure

In order to numerically solve equation (2.12) we must re-write it as two first order differential equations. We choose to integrate over column depth y as opposed to z, where $dy = -\rho dz$. The two resultant equations are

$$\frac{dT}{dy} = \frac{\mu}{\rho}\frac{(\ell+2)(\ell-1)}{R^2}\vec{\xi} - \left(\frac{B^2}{4\pi c^2 \rho} + 1\right)\omega^2\vec{\xi}, \tag{2.18}$$

and

$$\frac{d\vec{\xi}}{dy} = \frac{T}{\left(\mu + B^2/4\pi\right)\rho}, \tag{2.19}$$

where T is the horizontal traction defined as the force per unit area acting on a surface in the vertical direction (Carroll et al. 1986). It should be noted that we are assuming B^2 remains constant throughout the integration which allows us to replace $(B^2\rho/4\pi)(\partial^2\vec{\xi}/\partial y^2)$ with $(\partial/\partial y)(B^2\rho/4\pi)(\partial\vec{\xi}/\partial y)$.

Before integrating the above equations we must apply initial and boundary conditions. In the ocean we set $\vec{\xi} = 1$, $T = 0$, and $\mu = 0$ since shear waves can not exist in a fluid. We use a root finding program to invert our equation of state ($P(\rho) = P_n + P_e$) and solve for density as a function of pressure. We integrate over column depth from $y = 3.7 \times 10^{10}$ to $y = 8.8 \times 10^{12}$ g cm^{-2} which corresponds to the ocean density values mentioned in section (2.3.1). At the ocean/crust interface and at the transition from inner to outer crust we enforce continuity of the eigenfunction ($\vec{\xi}$) and the horizontal traction (T). We integrate from $y = 8.8 \times 10^{12}$ to $y = 5.0 \times 10^{15}$ g cm^{-2} in the outer crust and all the way down to $y = 2.8 \times 10^{18}$ g cm^{-2} in the inner crust, which again corresponds to the densities described for these regions in the previous section.

In order to solve for the ω eigenvalues we make an initial guess for the frequency, set the horizontal traction to zero at the top of the crust, and integrate equations (2.18) and (2.19) to the base. The resultant eigenfrequencies are those which satisfy the boundary condition at the base. By doing this we assume that the crust and core are completely decoupled which is not true. Recall from Chapter 1 that Glampedakis et al. (2006), Sotani et al. (2006, 2007), and Lee (2007) have looked into the effect of crust/core coupling on the modes. Despite this incorrect assumption we still find some interesting results.

2.3.3 Results

One of the first things we consider is the velocity of the different waves throughout the crust. We calculate the shear speed as well as the Alfvén speed for three magnetic field strengths, $B = 3 \times 10^{14}$ G, 6×10^{14} G, and 1×10^{15} G. See Figure (2–3) for a plot of these velocities against density. These results show that the shear speed dominates at the crust base ($\rho \approx 1 \times 10^{14}$ g cm^{-3}) where the Alfvén speed has died out. The peaks in the v_s curve ($\rho = 10^9 - 4 \times 10^{11}$ gcm^{-3}) arise from the discrete density values used throughout the outer crust (Haensel & Pichon 1994), whereas the smooth portion of the curve ($\rho = 4 \times 10^{11} - 10^{14}$ gcm^{-3}) arises from continuous density values throughout the inner crust (Douchin & Haensel 2001). Even though the shear waves travel faster than the Alfvén waves at the base, the magnetic waves can still have important effects on the modes if $v_A > v_s$ at the top of the crust. We show results of this later in the section.

In our models the shear modulus is $\mu = 1.45 \times 10^{25}$ ergs cm^{-3} at the top of the crust. Using the above condition $B/(4\pi\rho)^{1/2} > (\mu/\rho)^{1/2}$, implies B must be larger

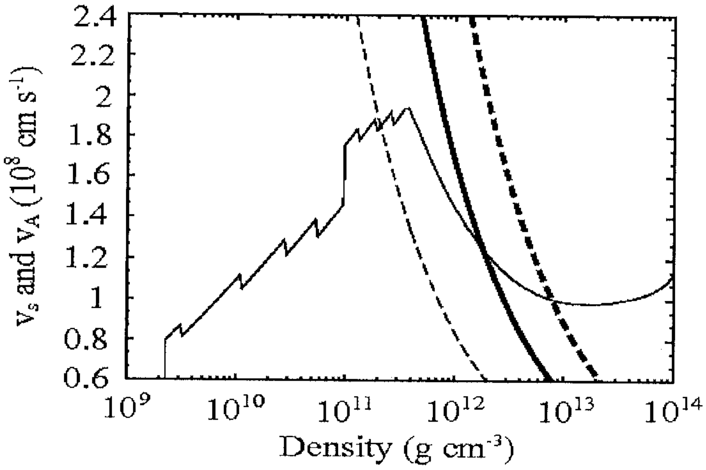

Figure 2–3: Shear speed v_s (thin solid line) and Alfvén speeds v_A for $B = 3 \times 10^{14}$ G (thin dashed line), 6×10^{14} G (thick solid line), and 1×10^{15} G (thick dashed line) as a function of density throughout the crust.

than 1.35×10^{13} G before the field will have an effect on these modes. This means for magnetic field strengths below this limit the ocean Alfvén waves will not be able to penetrate the crust. This is demonstrated in Figure (2–4) where we plot the absolute value of the eigenfunction ξ versus depth z for the $n = 0$, 1, and 4 modes when $B = 9 \times 10^{11}$ G (left panel) and $n = 0$, 2, and 4 modes for $B = 4 \times 10^{14}$ G (right panel). We keep $\ell = 2$ for each of these modes. Looking at the low field case first we notice that as soon as the wave reaches the top of the crust at $z \approx 1.2 \times 10^4$ cm the wave decays away. On the other hand, in the high field case we see that the Alfvén waves have no trouble crossing the ocean/crust interface where they become shear waves deep within the crust represented by the larger amplitudes at this depth. It should be noted that in both cases the $n = 0$ modes remain constant since they have no node and are independent of B.

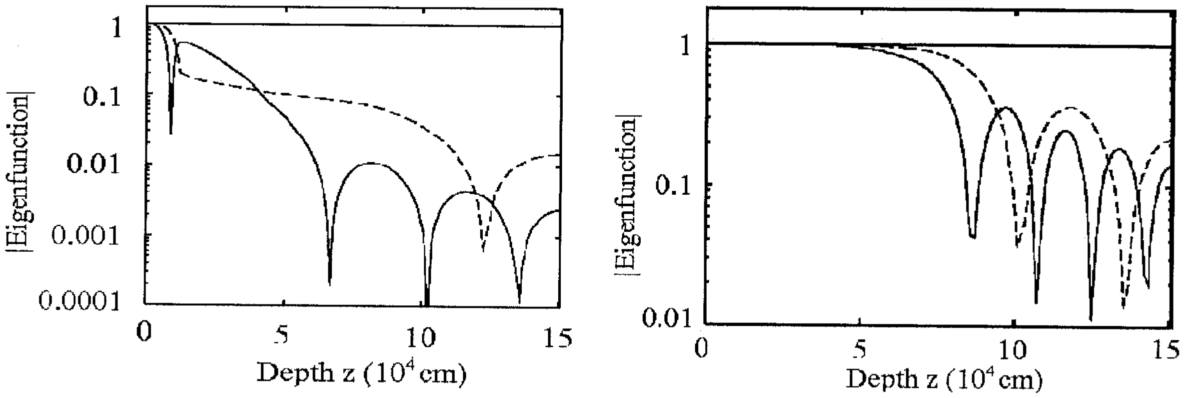

Figure 2–4: Absolute value of the eigenfunction ξ as a function of depth z for $\ell = 2$ for the $n = 0$ (constant thick solid line), 1 (dashed line), and 4 (solid line) modes for $B = 9 \times 10^{11}$ G (left panel), and $n = 0$ (constant thick solid line), 2 (dashed line), and 4 (solid line) modes for $B = 4 \times 10^{14}$ G (right panel). Note that the zero crossings are represented by cusps since we plot the absolute value of the displacement. Also notice how much larger the amplitudes are within the crust when B is large.

Now that we understand the displacements within the crust we would like to know if there is enough energy available to produce the observed QPOs during magnetar flares. In order to estimate this we follow Piro's (2005) approach and plot the energy density per logarithmic pressure, $dE/d\ln P = 2\pi R^2 \ell(\ell+1)\omega^2(\xi R)^2 P/g$, where we have multiplied our equation by R^2 to account for the fact that we set our initial displacement as $\xi = 1$ whereas Piro set his initial displacement as $\xi = R$. It should be noted that the ℓ scaling for this equation is correct as it comes from the angular integration over a sphere. The results for the $\ell = 2$ and $n = 0, 1,$ and 2 modes are given in Figure (2–5) for magnetic field strengths $B = 9 \times 10^{11}$ G (left panel) and $B = 4 \times 10^{14}$ G (right panel). Looking at the $n = 0$ mode which is the same in both plots, we see that the required excitation energy at the crust base is $\sim 10^{49}$ ergs which corresponds to an amplitude of $\xi \sim R$. Let's now consider what amplitude

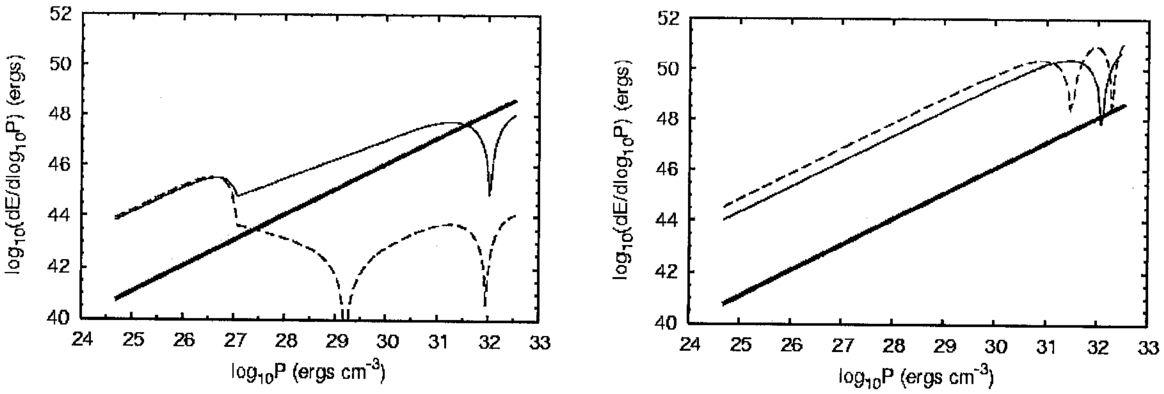

Figure 2–5: Energy density per logarithm pressure as a function of pressure for $\ell = 2$ and $n = 0$ (thick solid line), 1(thin solid line), and 2 (dashed line) modes for $B = 9 \times 10^{11}$ G (left panel) and $B = 4 \times 10^{14}$ G (right panel).

is required to excite these modes to the observed energies ($\sim 10^{44} - 10^{46}$ ergs). We know that the mode energy is proportional to ξ^2. This tells us that 10^{44} ergs of energy are needed to excite the lowest order modes to an amplitude of $\xi \sim 0.003R$ while 10^{46} ergs of energy are required for an amplitude of $\xi \sim 0.03R$. We therefore conclude that the observed energies from magnetar hyperflares are capable of exciting large amplitudes for the $n = 0$ modes, while more energy would be required to excite the higher order modes to the same amplitudes since their excitation energy at the base is higher. This is perhaps the reason that more lower order modes have been detected in comparison to the higher order ones.

All of our calculations up to this point have been on the neutron star surface. In order to compare our results to observations we must take gravitational redshift into account due to the energy loss of emitted photons. The redshift factor for a mass $M = 1.4\ M_{\odot}$ and radius $R = 1.2 \times 10^6$ cm is given by

$$\frac{\nu_{em}}{\nu_{obs}} = 1 + z = \left(1 - \frac{2GM}{Rc^2}\right)^{-1/2} = 1.235. \tag{2.20}$$

We may now plot our observed frequency values as a function of magnetic field strength. The results are given in Figure (2–6), where we plot the $n = 0$ modes for certain ℓ values as well as the $n = 1, 2, 3$, and 4 modes which we found to be independent of ℓ since we are only considering situations where $\ell \leq 13$. It should be noted that this plot is different from Piro's (2005) (see his Figure 3) in a couple ways. First of all we used the corrected $(\ell+2)(\ell-1)$ scaling as mentioned previously. This did not affect our $n > 0$ modes since they are independent of the harmonic index but it did affect our lowest order modes. The highest order modes also differ, where our mode crossings at low B occur for slightly lower magnetic field strengths than Piro's. Unfortunately we have not been able to find why this discrepancy occurs (private communications with Piro). One possibility is that it has to do with the boundary conditions. We tried to be as consistent with Piro's values as possible, but this could still be the culprit. We found that the top boundary conditions, those for the ocean and the top of the crust, had minimal effects on our results whereas the bottom boundary condition at the base of the crust had noticeable effects on our results. For example when we changed the bottom column depth from $y = 2.3\times10^{18} \rightarrow y = 2.8\times10^{18}$ g cm^{-2} (or equivalently $\rho = 8.6\times10^{13} \rightarrow \rho = 1.0\times10^{14}$ g cm^{-3}) our eigenfrequency ω increased by a factor of ~ 1000.

Despite these discrepancies we do still obtain some interesting results. Calculating our $n = 0$ modes using the corrected scaling we find an $\ell = 2$ fundamental

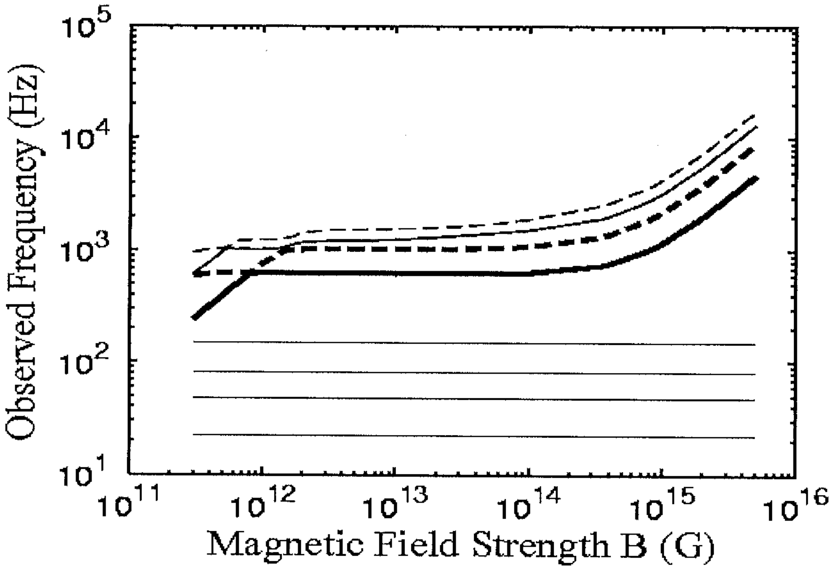

Figure 2–6: Observed frequency as a function of magnetic field strength B for the n = 0, 1 (thick solid line), 2 (thick dashed line), 3 (thin solid line), and 4 (thin dashed line) modes. For the $n = 0$ modes we have plot the results for $\ell = 2, 4, 7$, and 13 ($\ell = 2$ is the bottom line and $\ell = 13$ is the top horizontal line), whereas all the higher order modes have been calculated using $\ell = 2$.

frequency of 22 Hz, as opposed to 27.4 Hz which we find using Piro's scaling. This value is close to the analytic estimate given in section 2.2 (equation 2.15) which we calculated to be 24.6 Hz. Despite the fact that 22 Hz does not match any of the observed QPOs it is closer to the 18 and 26 Hz frequencies detected from SGR 1806-20. This would be a very exciting result since these frequencies have previously been difficult to explain. As already discussed, the base boundary conditions and therefore crust thickness are very important in determining the eigenvalues. This implies that adjusting the boundary conditions at the base could possibly result in a frequency of 18 Hz. However, more complicated neutron star models would have to be made before we could confirm these findings. While Piro associated his $\ell = 2$ frequency with the 30 Hz QPO emitted by SGR 1806-20, we find that our $\ell = 3$ frequency of $\sim$ 35.4 Hz is closer to this value than our $\ell = 2$ frequency. The index $\ell = 4$ gives a frequency of 47.4 Hz (50.0 Hz using Piro's scaling) which could be associated with SGR 1900+14's 53 Hz oscillation and it could also be associated with SGR 0526-66's 43.5 Hz QPO. We find $\nu = 82.2$ Hz (83.7 Hz with Piro's scaling) for the harmonic index $\ell = 7$ and $\nu = 93.7$ Hz for $\ell = 8$. We associate these with the 84 Hz QPO emitted by SGR 1900+14 and the 92 Hz QPO from SGR 1806-20, respectively. The last classification we make for the $n = 0$ modes is a frequency of 150.1 Hz (150.9 Hz with Piro's scaling) when $\ell = 13$ which we associate with the 150 Hz QPO from SGR 1806-20 and the 155 Hz oscillation from SGR 1900+14.

Next we discuss our $n > 0$ mode findings. For $n = 1$ we find that the horizontal branch (Figure 2–6) associated with the shear modes of the crust gives frequencies of $\sim$ 626.6 Hz for the modes independent of B. Piro (2005) also calculated this and when his paper was published no higher order modes had been found in any of the hyperflares data. Based on these calculations Piro recommended searching for QPOs in higher frequency ranges. Strohmayer & Watts (2006) did just that, uncovering a $\sim$625 and 1840 Hz oscillation in the tail of SGR 1806-20. It was very exciting that Piro's simplified model had predicted the $n = 1$ overtone. Our data also show that the 1840 Hz QPO could be associated with the $n = 3$ overtone. We also suggest that the less significant 2384 Hz oscillation detected by Strohmayer & Watts (2006) could be linked with the $n = 4$ mode. The fact that we find results similar to observations leads us to believe that the detected oscillations are produced by toroidal shear modes of the neutron star crust. Hopefully once more realistic models, taking into account a fuller neutron star structure, are employed the results will be even more consistent with the observations.

Now that we have mapped our mode frequencies to the observed SGR QPOs we continue by explaining the behavior of the modes in Figure (2–6). First of all the $n = 0$ modes exhibit no change with B, confirming the prediction that these modes depend on ℓ and do not depend on B. The more interesting behavior is exhibited by the overtone modes. On the far left of the plot (low B values) we see that the frequencies depend on B ($\omega \propto B$). The explanation for this dependence is that these waves are Alfvén waves trapped above the surface of the crust unable to penetrate through as discussed previously. If we remove the ocean from our calculations the $\omega \propto B$ relationship disappears as can be seen in Figure (2–7), where in this plot the horizontal branch due to the shear modes extends down to our lowest B values.

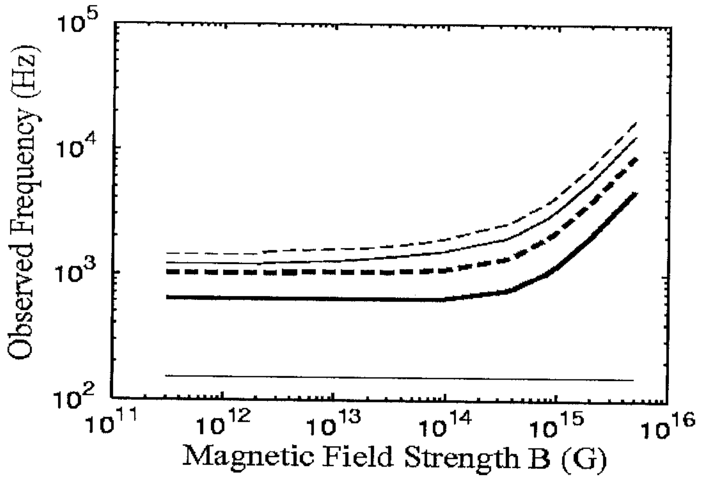

Figure 2–7: Observed frequency as a function of magnetic field strength B for the $n = 0$, 1 (thick solid line), 2 (thick dashed line), 3 (thin solid line), and 4 (thin dashed line) modes. These values were obtained when we removed the ocean from our calculations. For the $n = 0$ modes we have plot the result for $\ell = 13$ (bottom thin solid line), whereas all the higher order modes have been calculated using $\ell = 2$.

The next thing we notice in Figure (2–6) is the existence of mode (or avoided) crossings. This occurs when the wave changes character from an Alfvén wave to a shear wave or vice versa. This can be seen in Figure (2–6) at the point where the $n = 1$ and $n = 2$ modes almost cross. It appears as though the Alfvén wave ($\omega \propto B$) passes right through a shear wave (the horizontal line in the figure). On closer inspection we notice that the lines do not actually intersect, there is a forbidden region arising from the degeneracy of the modes, separating the $n = 1$ Alfvén and shear modes from the $n = 2$ overtones. This implies that for any line with constant radial number n, there may exist different types of waves.

We demonstrate this behavior by zooming in on the region around the avoided crossing for low B's between the $n = 1$ and $n = 2$ modes. This can be seen in Figure (2–8) where we plot the local energy density

$$\frac{E}{V} = \frac{1}{2}\rho\omega^2(\xi R)^2 + \frac{\delta B^2}{8\pi}, \tag{2.21}$$

as a function of column depth for three magnetic field strengths ($B = 6.55 \times 10^{11}$ G, $B = 8.0 \times 10^{11}$ G, and $B = 9.0 \times 10^{11}$ G) and their corresponding eigenfrequencies. In the top left panel when $B = 6.55 \times 10^{11}$ G and $\omega_{obs} = 519.7$ Hz for the $n = 1$ mode, the avoided crossing has not occurred at this point and we see that there exists one wave in the ocean which is purely Alfvén in character. Continuing down to the left middle plot where $B = 8.0 \times 10^{11}$ G and $\omega_{obs} = 624.1$ Hz we see that the mode is now mixed. There is an Alfvén wave wave in the ocean as well as a small crustal shear wave. Just after this, when $B = 9.0 \times 10^{11}$ G and $\omega_{obs} = 626.5$ Hz, the wave has completely changed character and is now a pure shear wave as can be seen on the left bottom panel of Figure (2–8). If we now look at the right side of this figure for the $n = 2$ mode we see the opposite behavior. The wave begins as a pure crustal shear wave in the top right panel when $B = 6.55 \times 10^{11}$ G and $\omega_{obs} = 626.8$ Hz, becoming mixed in character in the middle panel when $B = 8.0 \times 10^{11}$ G and $\omega_{obs} = 631.5$ Hz. Finally in the bottom right panel at $B = 9.0 \times 10^{11}$ G and $\omega_{obs} = 701.9$ Hz the wave has switched form completely and is now a pure ocean Alfvén wave.

The final thing to mention about Figure (2–6) is the transition from shear modes back to magnetic-dominated crustal modes at high B. We demonstrate this scaling with pure Alfvén waves in Figure (2–9), where we plot observed frequency versus B for the $n = 1$ mode for two cases. First we re-plot the $n = 1$ mode for our regular ocean/crust models which include the contribution from the shear modulus in the solid crust as well as the magnetic contribution. We also plot the $n = 1$ mode when $\mu = 0$ in the crust. By doing this we verify that the scaling for large B is consistent with the Alfvén waves ($\omega \propto B$). Referring back to Figure (2–3), we realize that even when the shear speed is greater than the Alfvén speed at the base of the crust the high magnetic field strengths do in fact have a large effect on the observable frequencies.

We conclude this chapter with one more calculation where we use our results and the observed frequencies from SGR 1806-20 to estimate the neutron star's crust thickness. Following the approach of Strohmayer & Watts (2006) we use our radius ($R = 1.2 \times 10^6$ cm), crust thickness ($\Delta R \approx 1.4 \times 10^5$ cm), and frequencies to obtain a proportionality constant from the ratio $\nu_{\ell,1}\Delta R/\nu_{2,0}R$, where the frequencies are denoted by $\nu_{\ell,n}$. Our frequencies are given by $\nu_{\ell,1} \approx 627$ and $\nu_{2,0} = 22$ Hz, which

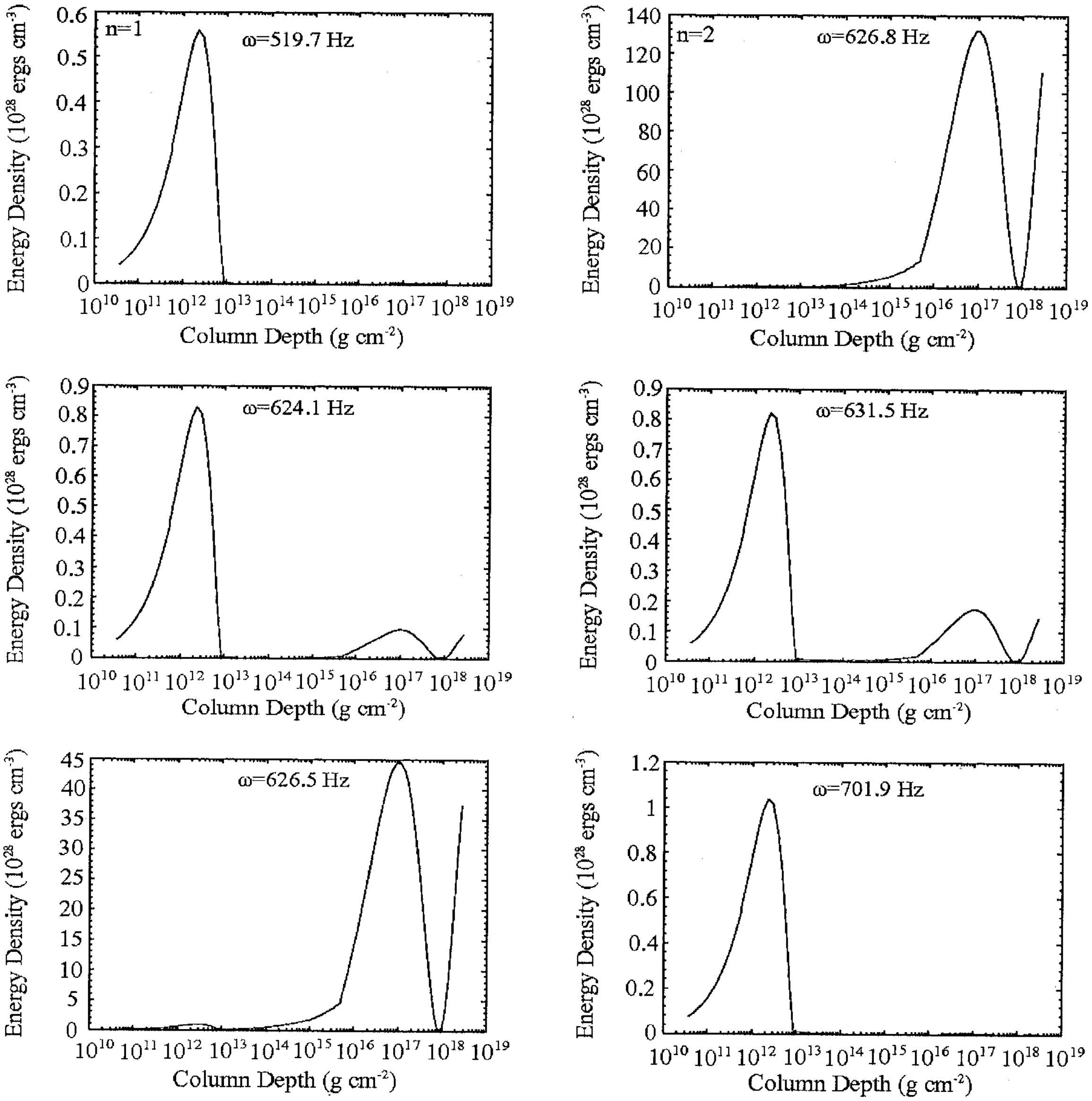

Figure 2–8: Local energy density versus column depth around the $n = 1$ (left panels) and $n = 2$ (right panels) avoided crossing between an Alfvén and shear mode for $B = 6.55 \times 10^{11}$ G (top panel), $B = 8.0 \times 10^{11}$ G (middle panel), and $B = 9.0 \times 10^{11}$ G (bottom panel). The corresponding redshifted eigenfrequencies are given for each plot.

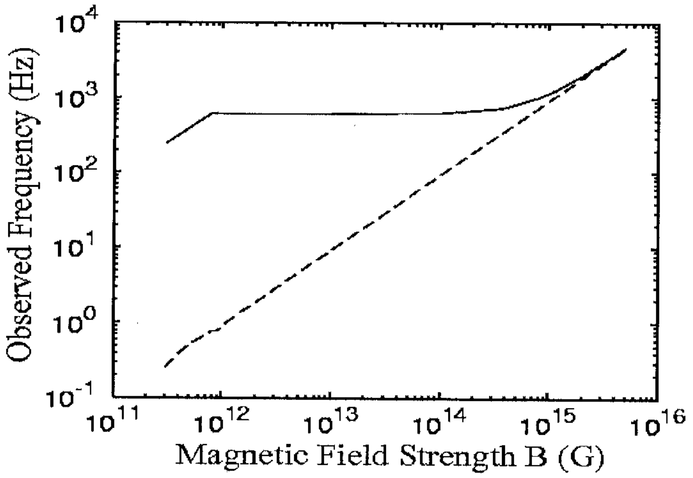

Figure 2–9: Observed frequency as a function of magnetic field strength B for $n = 1$ using our regular mixed shear and magnetic contributions (solid line) as well as a purely magnetic case (dashed line).

gives us a proportionality constant of 3.3. We may now use this constant along with the observed frequencies from SGR 1806-20, $\nu_{\ell,1} \approx 625$ and $\nu_{2,0} \approx 18$ Hz, to obtain an estimate for the neutron star's crust thickness. We find $\Delta R = 0.095R$. This is a very exciting result, implying that we may be able to use the observed QPOs to learn about the crustal properties of neutron stars!

CHAPTER 3
Non-Vertical Field Geometry Considerations

In this Chapter we extend the work done in Chapter 2 by considering a different field geometry. Magnetars have dipole or higher order magnetic fields which means a simple vertical field geometry is not an entirely adequate assumption. We begin by re-defining the key equations from Chapter 2 with the inclusion of our new poloidal field components (section 3.1). We proceed with our numerical calculations (section 3.1.1) which lead to more complicated results than originally expected. In order to better understand the effect that a non-vertical field has on these modes we continue with some analytic calculations (section 3.2), where we make two simple toy models (section 3.3 and 3.4) in an attempt to describe the behavior of the eigenfunctions.

3.1 The Main Equations for a New Field Geometry

We use the same equations given in section 2.1 but instead of having a constant vertical magnetic field we add a horizontal component. The field is now given by $\vec{B} = B_y\hat{y} + B_z\hat{z}$, where $B_y = B\cos\theta$ and $B_z = B\sin\theta$. The Lagrangian displacement is chosen to lie perpendicular to the plane of $\vec{B}$ and $\vec{g}$ and is therefore given by $\vec{\xi} = \xi_x\hat{x}$ for this field geometry. The displacement is still incompressible and satisfies the condition $\vec{\nabla}\cdot\vec{\xi} = 0$. The perturbed magnetic field is now given by

$$\delta\vec{B} = \left(\frac{\partial}{\partial y}(\xi_x B_y) + \frac{\partial}{\partial z}(\xi_x B_z)\right)_x, \tag{3.1}$$

which gives a perturbed current density of

$$\begin{aligned}\delta\vec{j} \;&=\; \frac{c}{4\pi}\Big[\Big(\frac{\partial^2}{\partial z\partial y}(\xi_x B_y) + \frac{\partial^2}{\partial z^2}(\xi_x B_z) + \frac{\omega^2}{c^2}\xi_x B_z\Big)_y \\ &\quad - \Big(\frac{\partial^2}{\partial y^2}(\xi_x B_y) + \frac{\partial^2}{\partial y\partial z}(\xi_x B_z) + \frac{\omega^2}{c^2}\xi_x B_y\Big)_z\Big].\end{aligned} \tag{3.2}$$

The resultant magnetic force term is

$$\delta\vec{j}\times\vec{B} = \frac{c}{4\pi}\Big[\frac{\partial^2}{\partial y^2}(\xi_x B_y^2) + \frac{\partial^2}{\partial z^2}(\xi_x B_z^2) + 2\frac{\partial^2}{\partial y\partial z}(\xi_x B_y B_z) + \frac{\omega^2}{c^2}\xi_x(B_y^2 + B_z^2)\Big]_x, \tag{3.3}$$

and the shear force term is

$$\frac{\partial}{\partial x_j}\delta\sigma_{xj} = \Big[\frac{\partial}{\partial y}\Big(\mu\frac{\partial \xi_x}{\partial y}\Big) + \frac{\partial}{\partial z}\Big(\mu\frac{\partial \xi_x}{\partial z}\Big)\Big]_x. \tag{3.4}$$

Combining equations (3.3) and (3.4) gives the full wave equation for a non-vertical magnetic field. By assuming an oscillatory time dependence and $\partial\vec{\xi}/\partial y \rightarrow ik_y\vec{\xi}$, the resultant equation is given by

$$-\rho\omega^2\vec{\xi} = -\mu k_y^2\vec{\xi} + \frac{\partial}{\partial z}\Big(\mu\frac{\partial\vec{\xi}}{\partial z}\Big) + \Big(ik_yB_y + B_z\frac{\partial}{\partial z}\Big)^2\frac{\vec{\xi}}{4\pi} + \frac{\omega^2}{c^2}\vec{\xi}(B_y^2 + B_z^2). \tag{3.5}$$

In order to numerically solve equation (3.5) it must be separated into two first order differential equations just like we did in Chapter 2. Unfortunately it is not as simple for this case since there is now an imaginary cross term arising from the two field components.

3.1.1 Numerical Procedure

In an attempt to work around the imaginary term and solve this equation numerically we consider a complex displacement which also gives rise to a complex perturbed magnetic field and perturbed current density. Equation (3.5) can now be written as two equations, one for the real part and one for the imaginary part. These are given by

$$-\rho\omega^2\xi_R = -\mu k_y^2\xi_R + \frac{\partial}{\partial z}\left(\mu\frac{\partial\xi_R}{\partial z}\right) + \frac{1}{4\pi}\left(-k_y^2B_y^2\xi_R + B_z^2\frac{\partial^2\xi_R}{\partial z^2} - 2k_yB_yB_z\frac{\partial\xi_I}{\partial z}\right) \quad (3.6)$$

and

$$-\rho\omega^2\xi_I = -\mu k_y^2\xi_I + \frac{\partial}{\partial z}\left(\mu\frac{\partial\xi_I}{\partial z}\right) + \frac{1}{4\pi}\left(-k_y^2B_y^2\xi_I + B_z^2\frac{\partial^2\xi_I}{\partial z^2} + 2k_yB_yB_z\frac{\partial\xi_R}{\partial z}\right) \quad (3.7)$$

respectively, where ξ_R and ξ_I denote the real and imaginary eigenfunctions and we have dropped the ω^2/c^2 term from our equations since $\omega << c$. Equations (3.6) and (3.7) can each be separated into two first order differential equations where we have again chosen to integrate over column depth y instead of vertical depth z. The two real equations are given by

$$\frac{dT_R}{dy} = \frac{\mu}{\rho}k_y^2\xi_R - \omega^2\xi_R + \frac{k_y^2B_y^2}{4\pi\rho}\xi_R - \frac{k_yB_yB_z}{2\pi}\frac{T_I}{(\mu + B_z^2/4\pi)\rho} \quad (3.8)$$

and

$$\frac{d\xi_R}{dy} = \frac{T_R}{(\mu + B_z^2/4\pi)\rho}, \quad (3.9)$$

where T_R and T_I are the real and imaginary horizontal tractions. The imaginary equations are similar to equation (3.8) and (3.9) and are given by

$$\frac{dT_I}{dy} = \frac{\mu}{\rho}k_y^2\xi_I - \omega^2\xi_I + \frac{k_y^2B_y^2}{4\pi\rho}\xi_I + \frac{k_yB_yB_z}{2\pi}\frac{T_R}{(\mu + B_z^2/4\pi)\rho} \quad (3.10)$$

and

$$\frac{d\xi_I}{dy} = \frac{T_I}{(\mu + B_z^2/4\pi)\rho}. \quad (3.11)$$

The next step is to apply the initial and boundary conditions. These are similar to the vertical field case except we now set the real and imaginary horizontal tractions to zero, the initial real displacement to one, and the imaginary displacement to zero at the top of the ocean. We make sure both displacements and tractions remain continuous throughout the ocean/crust and outer/inner crust interfaces and use the same method as Chapter 2 to solve for the eigenfrequencies, where ω must now satisfy the real and imaginary base boundary conditions. We search for the eigenvalues at different B and θ values, where $B_y = B\cos\theta$ and $B_z = B\sin\theta$ to gain insight into how the frequency depends on different field orientations. Unfortunately we are unable to find any ω satisfying both boundary conditions except for in the limiting case when $\theta = \pi/2$. In this situation the eigenfrequencies are the same as those found in Chapter 2 since in this limit the horizontal field component is zero. We end our numerical calculations at this point and continue with some analytic estimates in the next section in order to try and understand the physical picture of this problem a bit better.

3.2 Analytic Estimates for Pure Alfvén Waves

We begin by considering the pure Alfvén wave case where we set $\mu = 0$ throughout the crust. We still assume that $\partial\vec{\xi}/\partial y \rightarrow ik_y\vec{\xi}$ and we make an additional assumption that the displacement is given by $\xi_x \approx Dz/H$, where D is some function of y, z is the vertical distance, and H is the scaleheight. This implies that $\partial\xi_x/\partial z = D/H$ and $\partial^2\xi_x/\partial z^2 = 0$. The simplified wave equation in this situation is given by

$$-\rho\omega^2\frac{Dz}{H} = \frac{1}{4\pi}\Big(-k_y^2B_y^2\frac{Dz}{H} + 2B_yB_z\frac{\partial}{\partial y}\Big(\frac{D}{H}\Big)\Big). \tag{3.12}$$

By assuming that D is an oscillatory function of y given by

$$D = A\sin(ky) + B\cos(ky) = A\Big(\sin(ky) + \frac{B}{A}\cos(ky)\Big), \tag{3.13}$$

where A and B are unknown constants, and setting the vertical displacement to $z = H$ for simplicity equation (3.12) becomes

$$\begin{aligned} -\rho\omega^2 A\Big(\sin(ky) + \frac{B}{A}\cos(ky)\Big) &= \frac{1}{4\pi}\Big[-k_y^2 B_y^2 A\Big(\sin(ky) + \frac{B}{A}\cos(ky)\Big) \\ &+ \frac{2B_yB_z}{H}Ak\Big(\cos(ky) - \frac{B}{A}\sin(ky)\Big)\Big]. \end{aligned} \tag{3.14}$$

The next step is to equate the coefficients of $\cos(ky)$ and $\sin(ky)$, which gives two new equations

$$\Big(-\rho\omega^2 + \frac{k_y^2B_y^2}{4\pi}\Big)\frac{B}{A} = \frac{2B_yB_zk}{H} \tag{3.15}$$

and

$$\Big(-\rho\omega^2 + \frac{k_y^2B_y^2}{4\pi}\Big)\frac{A}{B} = \frac{-2B_yB_zk}{H}. \tag{3.16}$$

The constants A and B disappear when we multiply the above two equations. The resultant equation is

$$\Big(-\rho\omega^2 + \frac{k_y^2B_y^2}{4\pi}\Big)^2 = \frac{-4B_y^2B_z^2k^2}{H^2}, \tag{3.17}$$

which can be written in terms of the Alfvén speed in the y and z directions, $v_{A,y}^2 = B_y^2/4\pi\rho$ and $v_{A,z}^2 = B_z^2/4\pi\rho$,

$$\omega^4 - 2v_{A,y}^2k^2\omega^2 + (v_{A,y}k)^4 + \frac{4v_{A,y}^2v_{A,z}^2k^2}{H^2} = 0. \tag{3.18}$$

Solving the above quadratic equation for ω^2 gives us

$$\omega^2 = (v_{A,y}k)^2 \pm \frac{iv_{A,y}v_{A,z}k}{H}, \tag{3.19}$$

which is a complex solution. Taking the horizontal field limit ($B_z \rightarrow 0$) we recover the expected dispersion relation for Alfvén waves ($\omega^2 = v_{A,y}^2 k^2$). Although, if we now take the vertical field limit ($B_y \rightarrow 0$), ω^2 disappears which does not make sense since Chapter 2 considered only a vertical field and we calculated a real dispersion relation for that case. We realize that this term disappeared in the above calculations when we assumed that the displacement was proportional to z causing $\partial^2 \vec{\xi}/\partial z^2 \rightarrow 0$.

If we re-do this problem but do not assume a priori how $\vec{\xi}$ depends on z we recover the vertical term in the dispersion relation. We use the same approach as before but we assume $\vec{\xi} = f(z)(A\sin(ky) + B\cos(ky))$. The wave equation is now given by

$$\begin{aligned} -\rho\omega^2(A\sin(ky) + B\cos(ky)) &= -\frac{B_z^2}{4\pi} f''(z)(A\sin(ky) + B\cos(ky)) \\ &\quad -\frac{2B_yB_z}{4\pi} f'(z)k(A\cos(ky) - B\sin(ky)) \\ &\quad +\frac{B_y^2}{4\pi} f(z)k^2(A\sin(ky) + B\cos(ky)). \end{aligned} \tag{3.20}$$

Again we equate the coefficients of $\cos(ky)$ and $\sin(ky)$ and solve the quadratic equation for ω^2 which gives

$$\omega^2 = f(v_{A,y}k_y)^2 - f'' v_{A,z}^2 \pm \frac{2iv_{A,y}v_{A,z}k_y f'}{H}. \tag{3.21}$$

The result is still complex but we now have a real vertical field term as long as f'' is negative. In the limit $B_y \rightarrow 0$ or $B_z \rightarrow 0$ we uncover the expected dispersion relation for pure Alfvén waves in the z and y directions, respectively. Equation (3.21) also implies that as soon as the field is not perpendicular to $\hat{x}$ an imaginary cross term arises. We do not quite understand why the tilting of the field lines would give rise to an imaginary component. This is a topic that should be investigated further in the future.

3.3 Non-Vertical Field in a Box with Infinite Length

3.3.1 Pure Alfvén Waves

In an attempt to gain more insight into this problem we approach it from a different angle where we try to understand the behavior of the eigenfunction. We start again with equation (3.5) where this time we try to eliminate the imaginary cross term right away. This can be done by making a coordinate transformation, where by defining two new perpendicular axes, η and β, we can write y and z as functions of η and β given by

$$y = \eta \sin\theta + \beta \cos\theta \tag{3.22}$$

and

$$z = \eta \cos\theta - \beta \sin\theta. \tag{3.23}$$

Equivalently we can write η and β as functions of y and z, where

$$\eta = y \sin\theta + z \cos\theta \tag{3.24}$$

and

$$\beta = y \cos\theta - z \sin\theta. \tag{3.25}$$

See Figure (3–1) for a diagram of the new axes. We would now like to write the pure Alfvén wave equation in terms of these new coordinates. Writing equation (3.5)

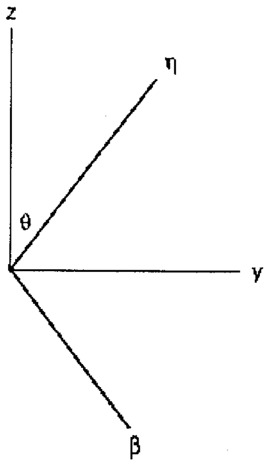

Figure 3–1: Diagram of the new coordinate system described by η and β, where the angle between η and β is 90 degrees and the angle between η and z is given by θ.

a slightly different way we get

$$\left(B_z\frac{\partial}{\partial z}+B_y\frac{\partial}{\partial y}\right)^2\xi_x=-4\pi\rho\omega^2\xi_x, \tag{3.26}$$

and if we let $B_y = B\sin\theta$ and $B_z = B\cos\theta$ equation (3.26) becomes

$$\left(\cos\theta\frac{\partial}{\partial z}+\sin\theta\frac{\partial}{\partial y}\right)^2\xi_x=-\frac{\omega^2}{v_A^2}\xi_x, \tag{3.27}$$

where $v_A^2 = B_{tot}^2/4\pi\rho$. Looking at the above equation we see that $(\cos\theta\partial/\partial z + \sin\theta\partial/\partial y)^2 = \partial^2/\partial\eta^2$. We can now write the wave equation in terms of the new coordinate η given by

$$\frac{\partial^2\xi_x}{\partial\eta^2}=\frac{-\omega^2}{v_A^2}\xi_x, \tag{3.28}$$

which is a second order differential equation with the solution

$$\xi_x(\eta,\beta)=A(\beta)\sin\left(\frac{\omega\eta}{v_A}\right)+B(\beta)\cos\left(\frac{\omega\eta}{v_A}\right), \tag{3.29}$$

where this oscillatory eigenfunction describes the waves traveling along the field lines in the η direction. We assume that A and B are functions of β which implies there is a specific β for each field line η.

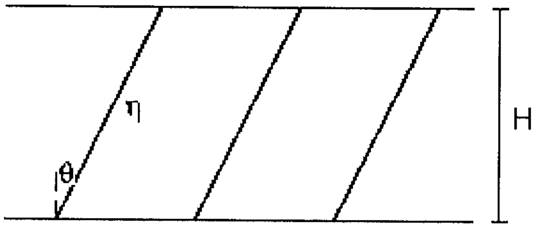

Figure 3–2: Two dimensional box with height H and infinite length where the field lines are defined by the coordinate $\eta = z/\cos\theta$.

Now that we have re-defined our coordinate system let's take a very simplistic toy model of a thin two dimensional box with height H in the z direction and infinite length in the y direction (see Figure 3–2). The total distance along the field lines is given by $\eta = H/\cos\theta$ in this simple system. We enforce continuity at the boundaries, $z = 0$ and $z = H$, which gives the condition $\xi_x(z = 0) = \xi_x(z = H) = 0$. Setting $z = 0$ in equation (3.23) gives

$$\eta_1 = \beta \tan\theta, \tag{3.30}$$

while setting $z = H$ gives

$$\eta_2 = \beta \tan\theta + \frac{H}{\cos\theta}. \tag{3.31}$$

We can now apply the boundary conditions in terms of η and β which gives us

$$
\begin{aligned}
A\sin\Big(\frac{\omega\beta\tan\theta}{v_A}\Big) + B\cos\Big(\frac{\omega\beta\tan\theta}{v_A}\Big) \quad = \quad & A\sin\Big(\frac{\omega\beta\tan\theta}{v_A}\Big)\cos\Big(\frac{\omega H}{v_A\cos\theta}\Big) \\
& +B\cos\Big(\frac{\omega\beta\tan\theta}{v_A}\Big)\cos\Big(\frac{\omega H}{v_A\cos\theta}\Big) \\
& -B\sin\Big(\frac{\omega\beta\tan\theta}{v_A}\Big)\sin\Big(\frac{\omega H}{v_A\cos\theta}\Big) \\
& = 0,
\end{aligned} \tag{3.32}
$$

and we have used the identities $\sin(A \pm B) = \sin A\cos B \pm \cos A\sin B$ and $\cos(A \pm B) = \cos A\cos B \mp \sin A\sin B$ to write it in the above form. We may now equate the coefficients of $\sin(\omega\beta\tan\theta/v_A)$ and $\cos(\omega\beta\tan\theta/v_A)$ to eliminate A and B from equation (3.32). The resultant dispersion relation is

$$
\omega = \frac{2\pi n v_A\cos\theta}{H} = v_A k, \tag{3.33}
$$

where $k = 2\pi(n\cos\theta/H)$ and $\lambda = (H/n\cos\theta)$. This is exactly what we expect for a pure Alfvén wave. The wavelength is equal to the total distance the wave can travel divided by the number of nodes. If we now go back to the first boundary condition $(A\sin(\omega\beta\tan\theta/v_A) + B\cos(\omega\beta\tan\theta/v_A) = 0)$ we can solve for the B/A ratio. We find $B/A = -\tan(\omega\beta\tan\theta/v_A)$. Plugging this into our eigenfunction (equation 3.29) we get

$$
\xi_x(\eta,\beta) = A(\beta)\left[\frac{\sin(\omega(\eta-\beta\tan\theta)/v_A)}{\cos(\omega\beta\tan\theta/v_A)}\right]. \tag{3.34}
$$

We would now like to transform $\xi_x(\eta,\beta) \to \xi_x(y,z)$. We know from equation (3.23) that $\eta - \beta\tan\theta = z/\cos\theta$ and from equation (3.25) that $\beta = y\cos\theta - z\sin\theta$. Also using $\omega/v_A = 2\pi n\cos\theta/H$ from equation (3.33) we obtain our final solution,

$$\xi_x(y,z) = A(\beta)\left[\frac{\sin(2\pi nz/H)}{\cos(\frac{2\pi n}{H}(y\sin\theta\cos\theta - z\sin^2\theta))}\right]. \tag{3.35}$$

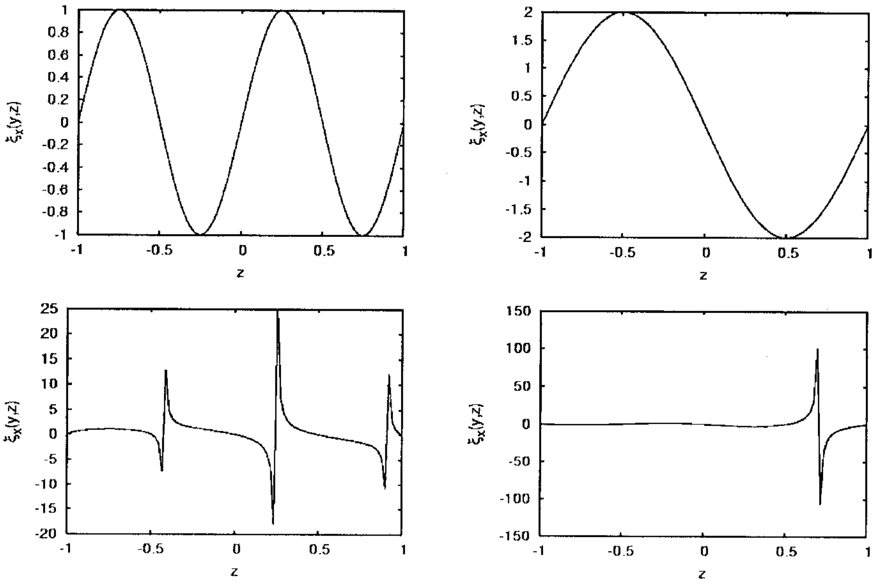

Figure 3–3: Eigenfunction versus z for $\theta = \pi$ (top left panel), $\theta = \pi/4$ (top right panel), $\theta = \pi/3$ (bottom left panel), and $\theta = \pi/8$ (bottom right panel).

We set $A = 1$ and plot this function, varying different parameters to see how it behaves. In Figure (3–3) we set n, H, and $y = 1$ and vary θ. We find that the function is sinusoidal when $\theta = 0$ and π (top left panel) since the denominator goes to one for these values of theta. When $\theta = \pi/4$ (top right panel) the function is still periodic but has a higher amplitude and fewer nodes. For all other angles the function is not periodic and has spikes occurring throughout its spectrum. These spikes probably arise when the denominator goes to zero, so for each choice of y there are particular z's where the argument of the cosine is $n\pi/2$ and $cos(n\pi/2) = 0 \Rightarrow$ displacement goes to infinity. We show this in Figure (3–3) for $\theta = \pi/3$ (bottom left panel) and $\pi/8$ (bottom right panel).

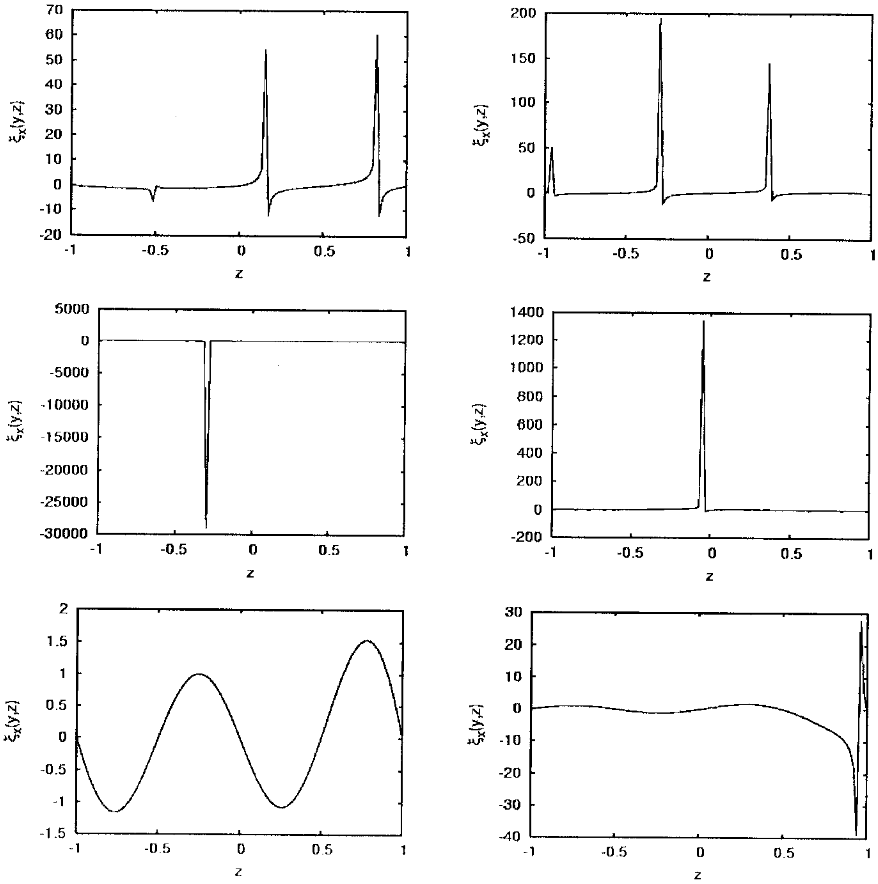

Figure 3–4: Eigenfunction versus z for $\theta = \pi/3$ for $y = 2$ (top left panel) and $y = 7$ (top right panel), and $\theta = \pi/8$ (middle and bottom panels), for $y = 2$ (middle left panel), $y = 12$ (middle right panel), $y = 7$ (bottom left panel), and $y = 11$ (bottom right panel).

In Figure (3–4) we plot the eigenfunction versus z again, but this time we set n and $H = 1$ and vary y. When $\theta = 0$ and π the result is the same as in the top left panel of Figure (3–3) for all y's since the y term vanishes for these values of theta. For certain angles, such as $\theta = \pi/3$ and $\pi/7$, the amplitudes change for different y values but the function maintains the same form. We show this in the two top panels of Figure (3–4) when $y = 2$ and 7 for $\theta = \pi/3$. On the other hand, when $\theta = \pi/8$ the function has three different forms. When $y = 2$, 6, and 8 there is a sharp spike in the negative direction, whereas for $y = 12$, 16, 18, and 22 the spike is now well above zero. When $y = 3$, 14, 17, and 20 the function is sinusoidal with increasing amplitude as z increases. The function begins with a positive slope. When $y = 4$, 7, 10, 13, and 21 the function has the same form except it begins with a negative slope. The final shape this function has when $\theta = \pi/8$ is two distinct spikes, one positive and one negative. This occurs when $y = 5$, 11, 15, and 19. We show these different behaviors for $\theta = \pi/8$ in the middle and bottom panels of Figure (3–4) when $y = 2$, 12, 7, and 11.

In Figure (3–5) we now set H and $y = 1$ and vary n. For $\theta = \pi/4$ (top panels) the function stays periodic and has $2n-1$ nodes. When $\theta = \pi/3$ and $\pi/8$ the function has the same form, where the number of spikes increases with increasing n and we see some periodic behavior between the spikes. We demonstrate this behavior in Figure (3–5) for $\theta = \pi/8$ when $n = 2$ (bottom left panel) and 5 (bottom right panel). These plots have given us an idea of how the eigenfunction behaves, although we should point out that we set $A = 1$ in all these calculations. In the future it would be beneficial to understand how A behaves as well.

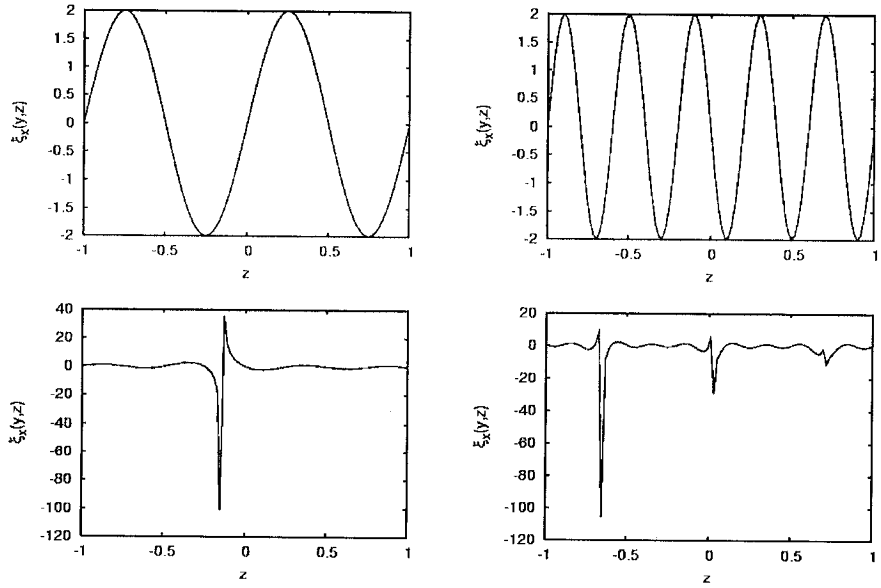

Figure 3–5: Eigenfunction versus z for $\theta = \pi/4$ for $n = 2$ (top left panel), and $n = 5$ (top right panel), and $\theta = \pi/8$ for $n = 2$ (bottom left panel), and $n = 5$ (bottom right panel).

3.3.2 Combined Shear and Alfvén Waves

Now that we have calculated the eigenfunction for a pure Alfvén wave we next turn to the shear wave solution, where for this case we set $B = 0$ and keep μ constant. Equation (3.5) for this situation becomes

$$\frac{\partial^2 \xi_x}{\partial y^2} + \frac{\partial^2 \xi_x}{\partial z^2} = \frac{-\rho\omega^2 \xi_x}{\mu}, \tag{3.36}$$

which has a separable solution of the form $\xi_x = [\cos(k_z z) + \sin(k_z z)][\cos(k_y y) + \sin(k_y y)]$. Using the same coordinate system described in the pure Alfvén case we find that $\partial/\partial y = \sin\theta\partial/\partial\eta + \cos\theta\partial/\partial\beta$ and $\partial/\partial z = \cos\theta\partial/\partial\eta - \sin\theta\partial/\partial\beta$. We can now write equation (3.36) in terms of η and β as

$$\frac{\partial^2\xi_x}{\partial\eta^2}+\frac{\partial^2\xi_x}{\partial\beta^2}=\frac{-\rho\omega^2\xi_x}{\mu}\Rightarrow v_s^2\frac{\partial^2\xi_x}{\partial\eta^2}+v_s^2\frac{\partial^2\xi_x}{\partial\beta^2}=-\omega^2\xi_x. \tag{3.37}$$

Now that we have solved for the shear and Alfvén equations (3.36) and (3.28) they can be combined to give the complete wave equation described in the new coordinate system,

$$v_s^2\left(\frac{\partial^2\xi_x}{\partial\eta^2}+\frac{\partial^2\xi_x}{\partial\beta^2}\right)+v_A^2\frac{\partial^2\xi_x}{\partial\eta^2}=-\omega^2\xi_x. \tag{3.38}$$

This equation looks familiar; it is the same as the analytic result we found in Chapter 2 for constant μ and B, except in a different coordinate system. This makes sense since the field lines are now directed along one axis, η. The solution is now separable so we write $\xi_x = f(\eta)g(\beta)$ and plug this eigenfunction into the above equation,

$$(v_A^2+v_s^2)\frac{f''}{f}+v_s^2\frac{g''}{g}=-\omega^2. \tag{3.39}$$

If we set

$$g''=-\frac{\sigma^2 g}{v_s^2}\text{ and } f''=-\frac{\omega^2-\sigma^2}{v_a^2+v_s^2}f \tag{3.40}$$

equation (3.39) is satisfied and the solution has the form

$$\begin{aligned}\xi_x(\eta,\beta) &= \left[A\sin\left(\frac{\sigma\beta}{v_s}\right)+B\cos\left(\frac{\sigma\beta}{v_s}\right))\right] \\ &\times\left[C\sin\left(\sqrt{\frac{\omega^2-\sigma^2}{v_a^2+v_s^2}}\eta\right)+D\cos\left(\sqrt{\frac{\omega^2-\sigma^2}{v_a^2+v_s^2}}\eta\right)\right],\end{aligned} \tag{3.41}$$

where the first term in brackets is $g(\beta)$ and the second term is $f(\eta)$.

We begin by applying our boundary conditions just for $f(\eta)$ and keeping $g(\beta)$ constant. This gives the same result as was found for the pure Alfvén case where at $z = 0$, $\eta_1 = \beta \tan\theta$ and at $z = H$, $\eta_2 = \beta\tan\theta + H/\cos\theta$. Putting these conditions back into equation (3.41) and setting the eigenfunction to zero at the boundaries, we can then equate the coefficients of $\sin(\sqrt{\omega^2 - \sigma^2/v_a^2 + v_s^2}\eta)$ and $\cos(\sqrt{\omega^2 - \sigma^2/v_a^2 + v_s^2}\eta)$ and eliminate the C/D ratio. We obtain the relation,

$$\omega^2 = \frac{4\pi^2 n^2 (v_a^2 + v_s^2)\cos^2\theta}{H^2} + \sigma^2. \tag{3.42}$$

Applying the boundary conditions again but this time for g(β) while keeping $f(\eta)$ constant, we find at $z = 0$, $\beta_1 = \eta\cot\theta$ while at $z = H$, $\beta_2 = \eta\cot\theta - H/\sin\theta$. Using the same approach as above we find

$$\sigma = \frac{2m\pi v_s \sin\theta}{H}. \tag{3.43}$$

Putting this into equation (3.42) we find the dispersion relation for the combined shear and Alfvén waves,

$$\omega^2 = \frac{4\pi^2}{H^2}(n^2(v_a^2 + v_s^2)\cos^2\theta + m^2 v_s^2 \sin^2\theta) \tag{3.44}$$

which is now a real solution. In order to eliminate as many of the constants in equation (3.41) as possible we use the boundary conditions for $f(\eta)$ and $g(\beta)$ to solve for the ratios D/C and B/A, where

$$\frac{D}{C} = -\tan\Big(\frac{2n\pi}{H}\eta\sin\theta\Big) \text{ and } \frac{B}{A} = -\tan\Big(\frac{2m\pi}{H}\eta\cos\theta\Big). \tag{3.45}$$

Plugging these ratios into equation (3.41) we solve for the eigenfunction in terms of η and β,

$$\begin{aligned}\xi_x(\eta,\beta) \;&=\; AC\Big[\sin\Big(\frac{\sigma\beta}{v_s}\Big) - \tan\Big(\frac{\sigma\eta\cot\theta}{v_s}\Big)\cos\Big(\frac{\sigma\beta}{v_s}\Big)\Big] \qquad (3.46)\\ &\times\Big[\sin\Big(\sqrt{\frac{\omega^2-\sigma^2}{v_a^2+v_s^2}}\eta\Big) - \tan\Big(\sqrt{\frac{\omega^2-\sigma^2}{v_a^2+v_s^2}}\beta\tan\theta\Big)\cos\Big(\sqrt{\frac{\omega^2-\sigma^2}{v_a^2+v_s^2}}\eta\Big)\Big].\end{aligned}$$

Using the definitions of η and β (equations 3.24 and 3.25) we transform this back into a function of y and z. The final solution is given by

$$\xi_x(y,z) = \frac{AC\sin\Big(-2m\pi z/H\Big)\sin\Big(2n\pi z/H\Big)}{\cos\Big(\frac{2m\pi}{H}(y\cos\theta\sin\theta + z\cos^2\theta)\Big)\cos\Big(\frac{2n\pi}{H}(y\cos\theta\sin\theta - z\sin^2\theta)\Big)}. \qquad (3.47)$$

We notice that the n dependence for this function is the same as the pure Alfvén case implying that the m dependence is caused by the shear waves.

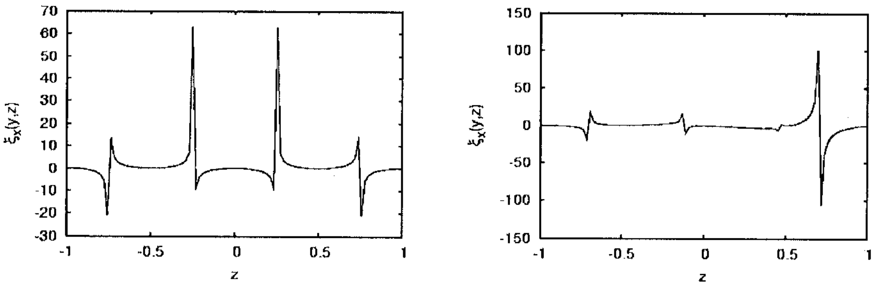

Figure 3–6: Eigenfunction versus z for $\theta = \pi$ (left panel) and $\theta = \pi/8$ (right panel). Comparing these plots to the pure Alfvén waves (Figure 3–3 top left and bottom right panels) we observe how the shear waves change the displacement.

We plot the total eigenfunction while varying different parameters, just as we did in the pure Alfvén situation. We set A and $C = 1$ for all of these calculations. In Figure (3–6) we keep n, m, H and $y = 1$ and plot the function for different values of theta. We notice for certain angles that the inclusion of the shear term changes the waveform dramatically, whereas for other values of *theta* it changes less, producing additional peaks as well as changing the amplitude of the original peaks. When $\theta = 0$ and π (left panel) the wave has changed completely, instead of being a sinusoidal function (see top left panel in Figure 3–3) it now has sharp peaks. The function is still symmetric about the $z = 0$ axis, but the waveform has changed appreciably. When $\theta = \pi/3$, $\pi/6$, $\pi/7$, and $\pi/8$ the function behaves similarly to the pure Alfvén case except there is now one more sharp peak and valley. Also, two of the peaks and valleys have been inverted for these values of theta. We show this for $\theta = \pi/8$ in the right panel of Figure (3–6) which can be compared to the pure Alfvén case displayed in the bottom right panel of Figure (3–3).

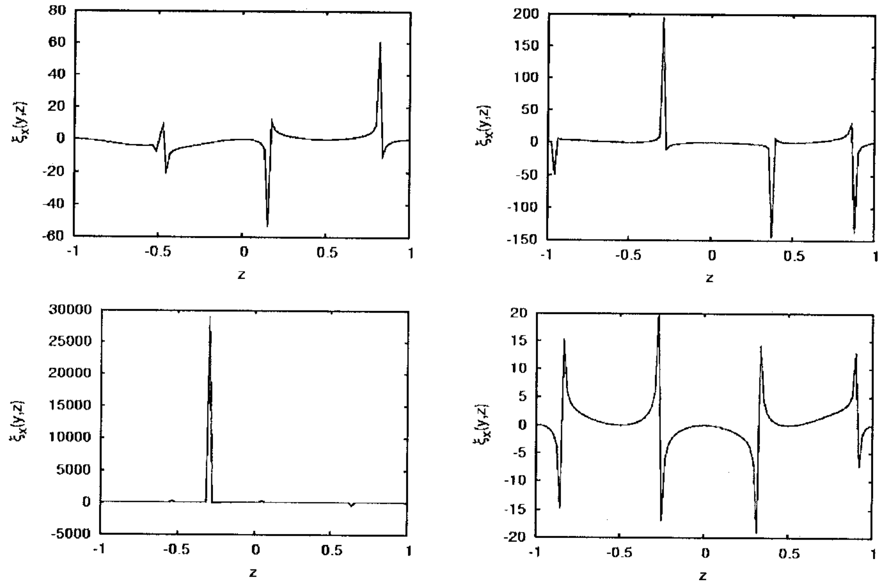

Figure 3–7: Eigenfunction versus z for $\theta = \pi/3$ for $y = 2$ (top left panel) and $y = 7$ (top right panel), and $\theta = \pi/8$ for $y = 2$ (bottom left panel), and $y = 7$ (bottom right panel).

We show the results of setting n, m, and $H = 1$ while varying y in Figure (3–7). When $\theta = \pi/3$ the eigenfunctions are similar to the pure Alfvén displacements. The addition of the shear term has changed the amplitude and sign of some peaks and has also produced additional peaks for certain y values. We plot the eigenfunction versus z for $y = 2$ (top left panel) and 7 (top right panel) which can be compared to the top two panels in Figure (3–4). For $\theta = \pi/8$ and $y = 2$ (bottom left panel) the sharp spike that was present in the pure Alfvén case has now flipped sign and there are a few additional small peaks (compare to the middle right panel of Figure 3–4). When $y = 7$ for the same angle the shear contribution has changed the waveform considerably, where there was a nice smooth function with increasing amplitude for the pure Alfvén waves (bottom right panel Figure 3–4), there are now many spikes present (bottom right panel Figure 3–7).

In our final variations to the eigenfunction we keep H and $y = 1$ and vary n and m. As expected the number of nodes increases with increasing n or m, while the waveforms do not change dramatically for different n and m values. In Figure (3–8) we plot the displacement for $\theta = \pi/3$ (top panels) and $\theta = \pi/8$ (bottom panels) for different combinations of m and n. We find the same results when interchanging m and n values, for example the displacement for $n = 1$ and $m = 2$ is equivalent to that when $n = 2$ and $m = 1$. We also notice that the amplitudes of the waveforms change slightly and we detect some periodicity between peaks as m and n increase.

As we mentioned in the pure Alfvén case, this has been helpful in giving us insight into what the eigenfunction looks like. This is just a first step in understanding how a different field geometry affects the oscillations. The next step would be

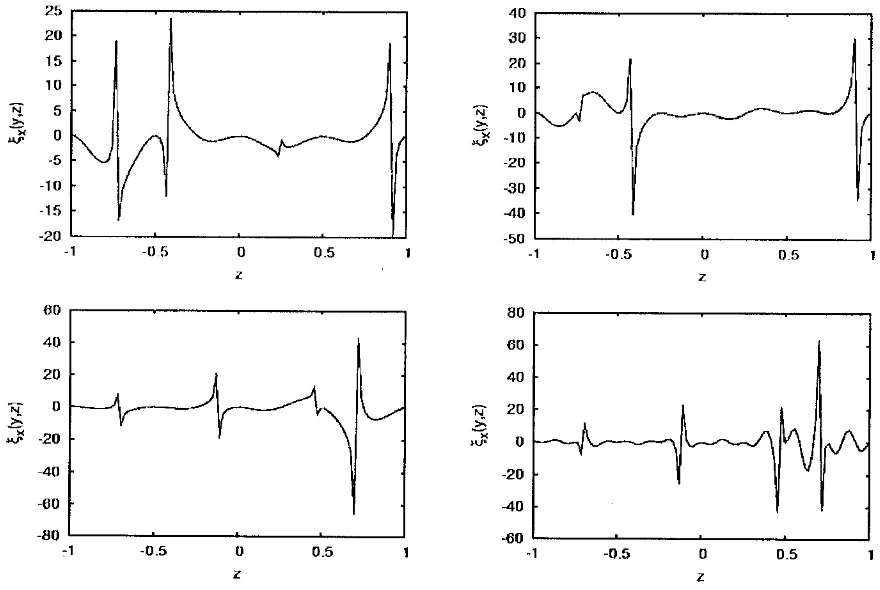

Figure 3–8: Eigenfunction versus z for $\theta = \pi/3$ for m=2, n=1 (top left) and m=2, n=2 (top right), and for $\theta = \pi/8$ for m=1, n= 2 (bottom left) and for m=6, n=6 (bottom right).

to do a full numerical calculation, solve for the eigenfrequencies, compare them to the observed QPOs, and solve for A and C. We already suggested that A and C depend on η and β. If this is true solving for these functions may get rid of the spike nature that we observed in Figures (3–3 → 3–8) which would then give us a complete picture of how the eigenfunction behaves.

3.4 Non-Vertical Field in a Closed Box

In this last section we make one more analytic calculation where we now consider a closed box of height H and length L instead of an infinitely long box, since the star is effectively a box with periodic boundary conditions at each end. We begin by breaking the box into three regions with one field line per region, where each field line is now a different length (Figure 3–9). We apply the boundary conditions in

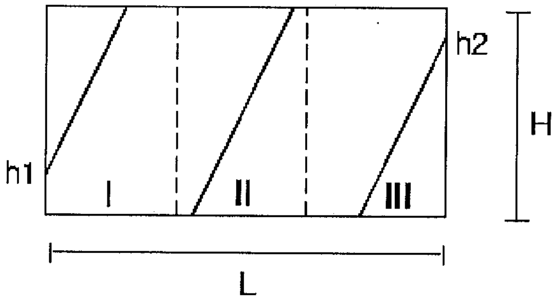

Figure 3–9: Two dimensional box with height H and length L, where the field lines are now a different length in each region.

each region by ensuring the eigenfunction remains continuous at the edges. In region one the boundary conditions occur when

$$\xi_x(z = h1) = 0 \Rightarrow \eta_1 = \beta \tan\theta + h1/\cos\theta, \tag{3.48}$$

and when

$$\xi_x(z = H) = 0 \Rightarrow \eta_2 = \beta \tan\theta + H/\cos\theta. \tag{3.49}$$

Using the same procedure as the previous section we solve the dispersion relation in this region to be

$$\omega^2 = \frac{4\pi^2}{(H - h1)^2}(n^2(v_a^2 + v_s^2)\cos^2\theta + m^2 v_s^2 \sin^2\theta). \tag{3.50}$$

Region two has the same dispersion relation as the result for the infinitely long box since the field line has a total length of $H/\cos\theta$. The result is given in equation (3.44). In the third region we apply the boundary conditions,

$$\xi_x(z = 0) = 0 \Rightarrow \eta_1 = \beta \tan\theta \tag{3.51}$$

and

$$\xi_x(z = h2) = 0 \Rightarrow \eta_2 = \beta \tan\theta + h2/\cos\theta, \tag{3.52}$$

which gives us a frequency of

$$\omega^2 = \frac{4\pi^2}{(h2)^2}(n^2(v_a^2 + v_s^2)\cos^2\theta + m^2 v_s^2 \sin^2\theta). \tag{3.53}$$

These results are what we would expect from looking at Figure (3–9); the dispersion relation in each region depends on the vertical height of the field line. This is interesting since it implies that for an infinite number of field lines there will be an infinite number of frequencies ⇒ a continuous spectrum! This result leads to some difficult questions which we discuss in the next chapter.

CHAPTER 4
Summary and Discussion

The first SGR hyperflare was detected on March 5th, 1979 (Mazets et al. 1979). Since then our knowledge regarding these bursts has grown immensely. The second and third hyperflares were observed in 1998 (Hurley et al. 1999) and 2004 (Israel et al. 2005). The QPOs produced by these flares prompted a great deal of research in attempts to understand the mechanisms underlying these events (see Chapter 1 for a review of the theoretical work on this subject). The proposed idea is that these flares occur when there is a sudden shift in the external magnetic footpoints of the star (Thompson & Duncan 1995). This displacement is caused by a build up of magnetic energy within the star which becomes so strong it fractures the crust while the magnetic field readjusts and reconnects. Since the field is anchored to the crust this leads to the release of huge amounts of energy, mostly in the form of gamma rays and x-rays, into the magnetosphere. It has been suggested (Duncan 1998) that seismic vibrations within the neutron star crust produce torsional oscillations which give rise to the QPOs observed during these hyperflares. If this theory is correct it implies that seismology can be used to uncover properties about the inner structure and composition of neutron stars.

We have focused on the torsional oscillation hypothesis throughout this thesis. The goal has been to gain insight into the QPOs detected during magnetar hyperflares and to understand how the magnetic field affects these frequencies. We have carried this out by making a simplified theoretical model of the neutron star crust and ocean which we have used to calculate the observed frequencies of these oscillations as a function of magnetic field strength for a vertical magnetic field (Chapter 2). In Chapter 3 we complicated the situation by considering how a non-vertical field geometry would affect this system. We conclude in this chapter by summarizing our work, discussing open issues, and suggesting future work on this topic.

4.1 Torsional Oscillations from SGRs

In Chapter 2 we modeled a neutron star crust and ocean with a vertical magnetic field. Piro (2005) recently calculated a similar model and our results agree well with his findings. We described the key equations for studying torsional oscillations which allowed us to make some analytic estimates, including the observed fundamental frequency of these modes. This gave us an observed frequency estimate of 24.6 Hz for the $n = 0$ and $\ell = 2$ mode in comparison to our numerical value of 22 Hz.

We proceeded by explaining the structure of the neutron star crust and ocean, where the pressure is dominated by nonrelativistic degenerate neutrons in the inner crust and relativistic degenerate electrons in the outer crust and ocean. We then calculated and compared the Alfvén and shear speeds throughout the crust, finding the shear speed to be much greater than the Alfvén speed at the crust base even for extremely high magnetic field strengths. We also found for field strengths less than 1.35×10^{13} G the Alvén waves will be trapped in the ocean. In this situation as soon as the waves try to penetrate the crust they decay away. On the other hand, when the field strength is high, the Alfvén waves travel through the crust and eventually become shear waves. We used the observed energies from SGR giant flares to estimate the amplitudes, finding that the bursts are capable of exciting appreciable amplitudes.

Our next step was to include gravitational redshift and calculate the observed frequencies as a function of magnetic field strength, which we then compared to the observed SGR QPO frequencies. We found that the $n = 0$ modes depend on ℓ and do not depend on B, whereas the $n > 0$ modes are independent of ℓ and dependent on B. For the $n = 0$ modes we associated our $\ell = 2$ and 3 modes with the 18, 26, and 30 Hz QPOs detected from SGR 1806-20. We linked our $\ell = 4$ mode with the 43.5 Hz QPO from SGR 0526-66 and the 53 Hz oscillation from SGR 1900+14, while we associated our $\ell = 7$ and 8 modes with the 84 Hz QPO from SGR 1900+14 and the 92 Hz oscillation from SGR 1806-20, respectively. The final $n = 0$ mode we compared to observations was $\ell = 13$, which we associated with the 150 Hz QPO from SGR 1806-20 and the 155 Hz oscillation from SGR 1900+14. The only source to emit frequency oscillations higher than 155 Hz was SGR 1806-20. We associated the $n = 1$ mode with the 625 Hz oscillation, and suggested that the $n = 3$ and $n = 4$ overtones could be associated with the 1840 Hz QPO and the less significant 2384 Hz oscillation.

We continued by describing the different regions on our plot of observed frequency versus magnetic field strength. We explained the concept of avoided crossings, arising from mode degeneracy, between shear and Alfvén waves. We demonstrated that different types of waves can exist for a specific radial number n by plotting the local energy density versus column depth around the avoided crossing between $n = 1$ and 2. We also described that for low and high magnetic field strengths the waves will be Alfvén-like in character. In the low field case this is due to the trapped ocean Alfvén waves unable to penetrate the crust, whereas in the high field case the large B causes the Alfvén wave to dominate over the shear wave.

We concluded Chapter 2 by using our results along with the observed QPOs for the $n = 0$, and $n = 1$, $\ell = 2$ modes from SGR 1806-20 to estimate the thickness of the neutron star crust. We found the crust thickness to be 9.5% compared to the stellar radius. If we continue observing higher order modes from SGR's than this will be a very useful probe into understanding the structure and composition of neutron stars.

Despite the fact that we used a simple plane-parallel model of the neutron star crust and ocean we were still able to associate our calculated frequencies with the observed QPOs produced during giant flares. This leads us to believe that torsional oscillations of the neutron star crust is a likely theory for the detected frequencies. In order to conclude that this is the underlying mechanism producing the observed QPOs some improvements should be made to our neutron star model. One suggestion is to include a more complex magnetic field geometry. We made an initial attempt to do this in Chapter 3 and will summarize our results in the next section. Additional considerations of the field geometry should include a complete spherical model of the neutron star including the core, crust, and ocean since the magnetic field couples the core to the crust. This model should also include general relativistic corrections, which we did not consider for our calculations. More accurate equations of state would be helpful as well. We used a cold, beta-equilibrium model of the neutron star which may not be entirely correct for young, hot magnetars. It would be beneficial to see how the composition depends on age and to understand what effect this has on the stars (Piro 2005).

Excitation and damping mechanisms should also be looked into, such as the damping effect of electromagnetic and gravitational radiation on the oscillations (Samuelsson & Andersson 2007). Viscous effects at the crust/core interface and dissipation in the neutron star core may also be important (Strohmayer & Watts 2007). Samuelsson and Andersson (2007) suggested that comparing the observations of SGR damping times ($\sim$ a few tens of seconds) to estimated damping times could help us understand these mechanisms within the sources. One final suggestion for future work would be to understand how x-rays and gamma rays are transmitted through the magnetosphere. Blaes et al. (1989) studied this before magnetars were known to exist and when equations of state were less accurate than they are today. Looking into this problem with our current knowledge on this subject could be extremely useful.

4.2 A Different Field Geometry

In Chapter 3 we re-defined our equations from Chapter 2 by adding a horizontal field component into our calculations. Changing the field geometry gave rise to an imaginary cross term in the wave equation for the combined shear and Alfvén waves. In an attempt to numerically solve this equation we considered a complex displacement and separated the second order differential equation into two real and two imaginary first order differential equations. We searched for eigenvalues satisfying the real and imaginary boundary conditions for different field strengths and geometries. Unfortunately, we were unable to simultaneously solve the real and imaginary boundary conditions except in the limiting case when the field was completely vertical. We did not continue with numerical calculations after this point. One suggestion for future work would be to apply different numerical techniques to this problem so as to solve for the eigenvalues and eigenfunctions.

Moving away from numerical calculations we made some analytical estimates with the goal of gaining more insight into the non-vertical field problem. Our first approach was to set the shear modulus to zero and consider pure Alfvén waves. We solved the dispersion relation for this situation and found that as soon as the field lines were tilted from the horizontal or vertical axis an imaginary cross term arose. We do not currently understand why this occurs and feel that further study on this subject would be useful.

The next step in our analytic calculations was to make a coordinate transformation in order to immediately eliminate the imaginary cross term from the wave equation. We made a simple toy model of an infinitely long box with a fixed height. We placed non-vertical field lines in this box, enforced continuity at the boundaries, calculated the dispersion relation, and solved for the eigenfunction for pure Alfvén waves as well as for the combined shear and Alfvén waves. We plot the eigenfunctions for both situations to get an idea of how the displacement behaves and to see how the inclusion of the shear waves affects the Alfvén waves. We found for most values of theta the eigenfunction was not periodic and exhibited large spikes in its spectrum. The addition of the shear term changed the waveform in different ways depending on the parameters. This work gave us some insight into the behavior of the eigenfunction. However, we must point out that we set certain functions (A and

C) equal to one for these calculations, which was a large simplification. We will not get a complete picture of how the eigenfunction behaves until we solve the problem completely. This calculation is encouraged for the future.

The final work we did in Chapter 3 was to take the box we had already considered and give it a finite height and length. We separated this closed box into three regions, with one field line per region each having a different length. Solving the dispersion relation for all the regions gave us three different frequencies depending on the vertical height of their corresponding field line. This calculation implies that if we have an infinite number of field lines we will have a continuous spectrum of modes! As mentioned at the end of Chapter 3 this result gives rise to some difficult questions. If in fact there is a continuous, as opposed to discrete, spectrum then what are we observing from these SGR hyperflares? The torsional oscillation model matched theory to observation quite well with the inclusion of a purely vertical magnetic field, so what is changing when the field is tilted away from the vertical axis? Also, if there is a continuous spectrum why are we detecting only certain frequencies during these flares. Perhaps only specific modes excite oscillations, but if this is true we must try and understand why this would be the case. Levin (2007) has recently made a first attempt at addressing these issues with a model of a coupled crust and core. The answers to these questions are unclear at this point and definitely a topic that requires further research. We hope that this work has given some insight into different field geometries for neutron star oscillations and we look forward to additional work on this topic.

References

Aptekar, R., et al. 1995, Space Sci. Rev., 71, 265

Barat, C., et al. 1983, A&A, 126, 400

Blaes, O., Blandford, R., Goldreich, P., & Madau, P. 1989, ApJ, 343, 839

Carroll, B. W., et al. 1986, ApJ, 305, 767

Cline, T. L., et al. 1982, ApJ, 255, L45

Cline, T. L., et al. 2000, ApJ, 531, 407

Cumming, A., Arras, P., Zweibel, E. 2004, ApJ, 609, 999

Douchin, F. & Haensel, P. 2001, A&A, 380, 151

Duncan, R. C. & Thompson, C. 1992, ApJ, 392, L9

Duncan, R. C. 1998, ApJ, 498, L45

Farouki, R. T., & Hamaguchi, S. 1993, Phys. Rev. E, 47, 4330

Feroci, M., Hurley, K., Duncan, R. C., & Thompson, C. 2001, ApJ, 549, 1021

Glampedakis, K., Samuelsson, L., & Andersson, N. 2006, MNRAS, 371, L74

Haensel, P. & Pichon, B. 1994, A&A, 283, 313

Hansen, C. J., & Cioffi, D. F. 1980, ApJ, 238, 740

Hansen, C. J., Kawaler, S. D., & Trimble, V. 2004, Stellar Interiors Physical Principles, Structure, and Evolution Second Edition (Springer-Verlag New York, Inc.)

Heger, A., et al. 2003, ApJ, 591, 288

Heger, Woosley, & Spruit 2005, ApJ, 626, 350

Hurley, K., et al. 1992, A&AS, 92, 401

Hurley, K., et al. 1999, Nature, 397, 41

Israel, G. L., et al. 2005, ApJ, 628, L53

Kouveliotou, C., et al. 1993, Nature, 362, 728

Kouveliotou, C., Kippen, M., Woods, P., Richardson, G., Connaughton, V., & McCollough, M. 1998, IAU Circ. 6944

Lee, U. 2007, MNRAS, 374, 1015

Levin, Y. 2006a, MNRAS, 368, L35

Levin, Y. 2006b, MNRAS, 377, 159

Mackie, F. D., & Baym, G. 1977, Nucl. Phys. A, 285, 332

Mazets, E. P., et al. 1979a, Nature, 282, 587

Mazets, E. P., Golenetskii, S. V., & Gur'yan, Y. A. 1979b, Sov. Astron. Lett., 5, 343

McDermott, P. N., Van Horn, H. M., & Hansen, C. J. 1988, ApJ, 325, 725

Meegan, C., et al. 1996, ApJS, 106, 45

Messios, N., Papadopoulos, D. B., & Stergioulas, N. 2001, MNRAS, 328, 1161

Palmer, D.M., et al. 2005, Nature, 434, 1107

Piro, A. L. 2005, ApJ, 634, L153

Samuelsson, L., & Andersson, N. 2007, MNRAS, 374, 256

Shapiro, S. L., & Teukolsky, S. A. 1983, Black Holes, White Dwarfs, and Neutron Stars The Physics of Compact Objects (Toronto: John Wiley & Sons, Inc.)

Sotani, H., Kokkotas, K. D., Stergioulas, N., & Vavoulidis, M. 2006, MNRAS, submitted [astro-ph/0611666v1]

Sotani, H., Kokkotas, K. D., & Stergioulas, N. 2007, MNRAS 498, 261

Strohmayer, T. E., Ogata, S., Iyetomi, H., & Van Horn, H. M. 1991, ApJ, 375, 679

Strohmayer, T. E., & Watts, A. L. 2005, ApJ, 632, L111

Strohmayer, T. E., & Watts, A. L. 2006, ApJ, 653, 593

Terasawa, T., et al. 2005, Nature, 434, 1110

Thompson, C., & Duncan, R. C. 1995, MNRAS, 275, 255

van der Klis, M. 2006, to appear in Compact stellar X-ray sources, Lewin & van der Klis (eds), Cambridge University Press [astro-ph/0410551v1]

Wang, Z., Chakrabarty, D., & Kaplan, D. L. 2006, Nature, 440, 772

Watts, A. L., & Reddy S. 2006, preprint [astro-ph/0609364v1]

Watts A. L., & Strohmayer, T. E. 2006, ApJ, 637, L117

Watts A. L., & Strohmayer, T. E. 2007, preprint [astro-ph/0612252v2]

Woods, P. M., et al. 1999, ApJ, 519, L139

Woods, P. M., & Thompson, C. 2004, in press [astro-ph/0406133v3]